

Anomalously low $\delta^{18}\text{O}$ values of high-latitude Permo-Triassic paleosol siderite

Zachary D. Richard^{a,*}, David Pollard^b, Lee R. Kump^a, Timothy S. White^b

^a Department of Geosciences, The Pennsylvania State University, University Park, PA 16802-2712, USA

^b Earth and Environmental Systems Institute, The Pennsylvania State University, University Park, PA 16802-6813, USA



ARTICLE INFO

Keywords:

Oxygen isotopes
Paleoclimate
GENESIS
Wetlands
Hydrologic cycle
Seasonality

ABSTRACT

The most severe extinction in Earth history occurred during a time of extreme climate change, caused in part by a massive release of carbon into the atmosphere. Isotopic measurements of siderite occurring in paleosols during intervals of global warming suggest high-latitude depletions in $\delta^{18}\text{O}$ of precipitation, often attributed to an amplified hydrologic cycle. Here, Late Permian and Early Triassic paleosol siderite from Alaska, Antarctica, eastern Australia, Siberia, and South Africa indicate similar or greater meridional gradients in siderite $\delta^{18}\text{O}$ compared to other past warm intervals.

An isotope-tracer-enabled version of the Global Environmental and Ecological Simulation of Interactive Systems (GENESIS) general circulation model (GCM) was used to compare to siderite $\delta^{18}\text{O}$ data. The model, when deriving siderite $\delta^{18}\text{O}$ at a specified paleoatmospheric CO_2 concentration of $12.7 \times$ the preindustrial atmospheric level (PAL), matches a small subset of relatively less depleted high-latitude siderites but does not produce the conditions necessary to explain the most depleted siderite $\delta^{18}\text{O}$ values. Siderite has been thought to record mean annual precipitation $\delta^{18}\text{O}$, though this study suggests that many may not. A seasonal bias, where siderite growth occurs in the summertime in wetlands that receive most of their recharge from melting winter precipitation, may be responsible. GENESIS indicates soil moisture recharge during the spring ahead of the rainy season for high-latitude Permo-Triassic (PT) siderite localities that reach below freezing winter temperatures. Drainage from high altitude regions throughout the growing season may also be responsible. Biological cloud feedbacks and monsoon-related amount effects are not likely the cause for low siderite $\delta^{18}\text{O}$ because the enrichment of water vapor $\delta^{18}\text{O}$ associated with warming is too significant.

1. Introduction

Efforts to reconstruct paleoclimates have relied predominately on marine proxy records such as conodonts, brachiopods, and foraminifera because of their typically superior preservation and abundance. Terrestrial proxies, specifically paleosol carbonates, can be equally important because they can record the oxygen isotopic signatures of paleorainfall (e.g., Ludvigson et al., 1998), useful for understanding atmospheric circulation, patterns in precipitation, and terrestrial temperatures. This information is valuable for the end-Permian because it can help further refine and explain the causes of mass extinction and the ecological consequences of extreme climate change.

One paleosol carbonate, siderite (FeCO_3), can be a particularly reliable paleoclimate proxy due to its resistance to diagenetic alteration, and by virtue of its formation environment. Siderite can be found within coals (e.g., Faure et al., 1995, 1996; Passey, 2014), intensively weathered paleosols with significant smectite or kaolinite content

(White et al., 2000, 2001), and gleyed wetland paleosols (e.g., Ufnar et al., 2004a). In freshwater depositional settings, siderite precipitates in equilibrium with meteoric water (Ludvigson et al., 1998). Because of its formation in water saturated soils, siderite does not require an evaporative fractionation correction typical of carbonates that form in well-drained or seasonally dry soils, like calcite (e.g., Gabitov et al., 2012; Kele et al., 2011).

Siderite $\delta^{18}\text{O}$ is determined by the surface temperature and $\delta^{18}\text{O}$ of the water (presumably precipitation) that the siderite equilibrates with at the time of its formation. Both surface temperature and $\delta^{18}\text{O}$ of precipitation are assumed to be equivalent to mean annual values. The $\delta^{18}\text{O}$ content of siderite is temperature sensitive, and is given by the temperature-dependent siderite-water fractionation equation of Zhang et al. (2001):

$$1000 \ln \alpha_{\text{siderite-water}} = 2.56 \times 10^6 (T^{-2}) + 1.69 \quad (1)$$

where α is the fractionation factor between siderite and water, and T is

* Corresponding author.

E-mail address: zachrichard021@gmail.com (Z.D. Richard).

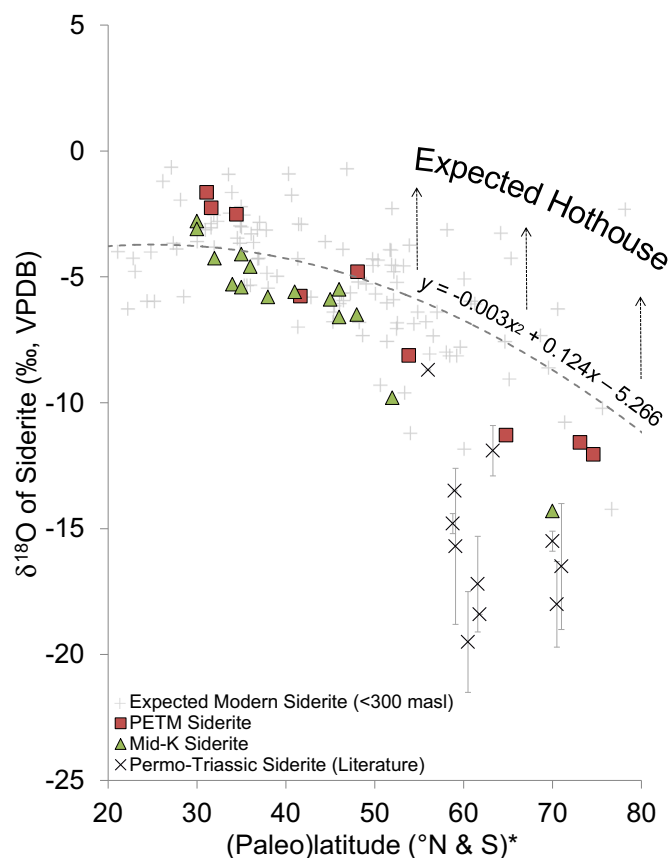


Fig. 1. Literature siderite $\delta^{18}\text{O}$ values for the Paleocene-Eocene thermal maximum (PETM) (White et al., 2017), middle Cretaceous (Mid-K) (White et al., 2001) and Permo-Triassic (see Table 1 for references). Expected modern siderite and best-fit gradient (dashed line) is calculated from the IAEA/WMO dataset from Rozanski et al. (1993), filtered to only include low altitude (< 300 m above sea level) localities most likely to host wetlands. All three hothouse periods have low siderite $\delta^{18}\text{O}$ values at high latitude, which is the opposite of what we expect for warm climates with low thermal gradients. *x-axis combines N and S latitudes in order to more easily compare samples from separate hemispheres. Fig. 5 and Fig. 8 are also displayed in this way.

the surface temperature in Kelvin. Note that increasing T lowers α , thereby reducing the difference in $\delta^{18}\text{O}$ between siderite and formation waters.

Observations of paleosol siderite from the Paleocene-Eocene Thermal Maximum (PETM) (White et al., 2017) and the Albian-Cenomanian boundary of the Mid-Cretaceous (e.g., White et al., 2001;

Ufnar et al., 2002, 2004b; Poulsen et al., 2007) show that the $\delta^{18}\text{O}$ content is depleted at high latitudes ($\sim 0.25\text{‰}$ per degree latitude). Literature data of PT siderite $\delta^{18}\text{O}$ suggests a similar high-latitude depletion trend, but perhaps at a more significant scale (Fig. 1, Table 1).

The observed meridional siderite $\delta^{18}\text{O}$ gradients (Fig. 1), considered as capturing a signal of global-scale atmospheric hydrologic effects, mimic what would be expected for siderite formation in climates similar to the modern. In warm, ice-free climates of the past, like the PT, PETM, and Mid-Cretaceous, temperature decreased less between equator and pole, the kinetic fractionation during evaporation was reduced, and Rayleigh distillation was not as dominant (e.g., Speelman et al., 2010; Krishnan et al., 2014). Consequently, the $\delta^{18}\text{O}$ content of water vapor was higher, particularly at high latitudes, relative to the modern. Therefore, a gradual siderite $\delta^{18}\text{O}$ meridional gradient is expected during hothouse intervals.

In order to produce steep siderite $\delta^{18}\text{O}$ meridional gradients on a warm Earth, a mechanism is required to lower (deplete) precipitation $\delta^{18}\text{O}$, or otherwise the $\delta^{18}\text{O}$ content of water from which the siderite precipitated. One suggestion is that the observed high-latitude depletions in siderite $\delta^{18}\text{O}$ during hothouse intervals are related to intensified atmospheric hydrological cycling (e.g., White et al., 2001) in which there is an increase in vapor isotopic fractionation. This hypothesis has not been supported by GCMs with high levels of $p\text{CO}_2$ (e.g., Poulsen et al., 2007; Speelman et al., 2010; Winnick et al., 2015). Other hypotheses include amount effects from increased precipitation rates (Ludvigson et al., 1998; White et al., 2001; Ufnar et al., 2002, 2004b), enriched $\delta^{18}\text{O}$ of tropical seawater as well as low relative humidity in the subtropics (Suarez et al., 2011), and local variability in climate, topography, and sea level (Poulsen et al., 2007).

An additional hypothesis, rainout effects from a biological cloud feedback mechanism, may also be considered. Late-Permian warming, stratification, and thus limited available nutrients in surface oceans may have reduced the abundance of marine phytoplankton, a source of dimethyl sulfide in the atmosphere that would have served as the predominate origin of cloud condensation nuclei (CCN) in a pre-anthropogenic world (Andreae, 2007; Charlson et al., 1987). Less atmospheric dimethyl sulfide, and therefore fewer CCN, reduces cloud abundance, increases cloud transparency, and greatly reduces the cloud cooling feedback (Winguth et al., 2015). Kump and Pollard (2008) argue that the reduction in available CCN, or the CCN effect, may account for the increased global warmth suggested in proxy data for the Cretaceous, where the observed warmth from proxies is poorly supported by atmospheric CO_2 estimates.

In a CCN-limited world, storms may be short-lived because drops would carry more water to offset elevated evaporation rates (e.g., Bohren, 1985; Kerminen et al., 2012). Conceivably, this fast CCN effect-derived rainout may produce greater fractionations associated with the

Table 1
Literature-derived siderite.

| Location | Paleolatitude (°N) ^a | Formation | Age | $\delta^{18}\text{O}_{\text{VPDB}}/\text{‰}$ | $\delta^{13}\text{C}_{\text{VPDB}}/\text{‰}$ | Reference |
|---|---------------------------------|--------------|----------------|--|--|-----------------------|
| Waterberg Coalfield, South Africa | –56 | Beaufort Fm. | Late Permian | –8.7 | –15.1 | Faure et al., 1995 |
| Northern Bowen Basin (KL11 & DR16 Bores) | –58.8 | Rangal Coal | Late Permian | –14.8 ± 0.4 | –1.8 ± 0.4 | Uysal et al., 2000 |
| Northern Bowen Basin (GCR Bore) | –59 | Rangal Coal | Late Permian | –13.5 | +5.6 | Uysal et al., 2000 |
| Galilee Basin, Degulla Bores | –59.1 | – | Late Permian | –15.7 ± 3.1 | +5.7 ± 3.7 | Gould and Smith, 1979 |
| Blackwater Area Bores, Central Bowen Basin | –60.5 | – | Late Permian | –19.5 ± 2.0 | +3.8 ± 5.4 | Gould and Smith, 1979 |
| Baralaba-Theodore Area, Central Bowen Basin | –61.6 | – | Late Permian | –17.2 ± 1.9 | +5.5 ± 1.3 | Gould and Smith, 1979 |
| Brolga No. 1 well, Cooper Basin | –61.8 | – | Late Permian | –18.4 | –1.3 | Gould and Smith, 1979 |
| Southern Bowen Basin | –63.3 | Rewan Group | Permo-Triassic | –11.9 ± 1.0 | –7.2 ± 7.2 | Baker et al., 1996 |
| Fassifern Seam & Dencan Bore, Sydney Basin | –70 | – | Late Permian | –15.5 ± 0.4 | +3.8 ± 0.6 | Gould and Smith, 1979 |
| Southern Coalfield, Sydney Basin | –70.5 | – | Late Permian | –18.0 ± 1.7 | +3.1 ± 1.0 | Gould and Smith, 1979 |
| Tahmoor & Metropolitan collieries, Sydney Basin | –71 | Bulli Coal | Latest Permian | –16.5 ± 2.5 | +4.0 ± 1.1 | Botz et al., 1986 |

^a Approximate PT paleolatitude (confidence ± 5°).

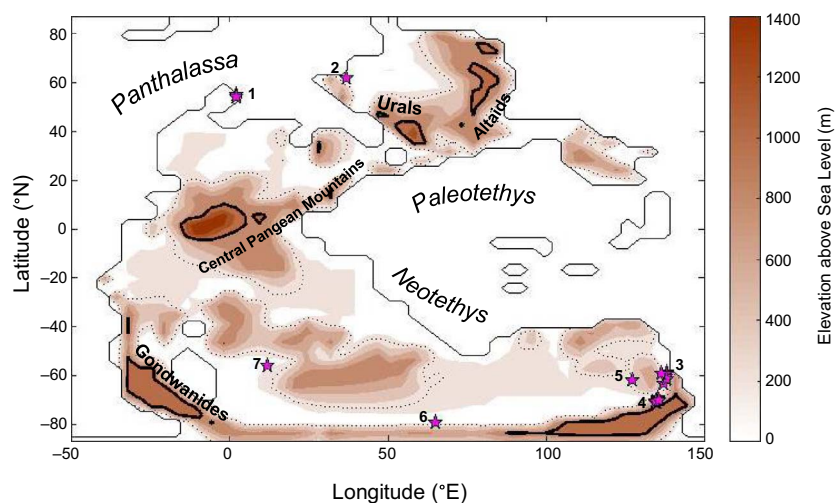


Fig. 2. Late Permian geographic and topographic reconstruction of Pangea used in the GENESIS model, modified from Ziegler et al. (1997). Labeled are the major existing bodies of water and mountain ranges. Dark contour lines indicate 1000 masl, and the dotted contour indicates 300 masl. Pink stars mark the approximate locations of samples used in this study, both those from the literature and newly investigated. (1) North Slope, Alaska; (2) Kotuy river, Siberia; (3) Bowen and Galilee Basins, Queensland, Australia; (4) Sydney and Gunnedah Basins, New South Wales, Australia; (5) Cooper Basin, Queensland, Australia; (6) Graphite Peak, Antarctica; (7) Waterberg Coalfield, northern Karoo Basin, South Africa. (For interpretation of the references to color in this figure legend, the reader is referred to the web version of this article.)

amount effect, and may increase the meridional $\delta^{18}\text{O}$ gradient by depleting precipitation $\delta^{18}\text{O}$ faster relative to clouds with more abundant CCN and smaller droplets. This is tested in GENESIS by making cloud droplet sizes 30% larger and therefore more than doubling the rainout efficiency factor (Kump and Pollard, 2008).

In this study, literature-reported siderite $\delta^{18}\text{O}$ and Late Permian/Early Triassic paleosol siderite samples spanning $\sim 25^\circ$ of PT paleolatitude were used to reconstruct the trend of siderite $\delta^{18}\text{O}$ versus paleolatitude. The sample localities and respective $\delta^{18}\text{O}$ values were then compared to GENESIS climate model simulations in an effort to explain the siderite $\delta^{18}\text{O}$ data and to examine and evaluate the possible causes or mechanisms that lead to high-latitude siderite $\delta^{18}\text{O}$ depletions during hothouse intervals.

2. Methods

2.1. Preparation and analysis of paleosol siderite

Thirteen siderite-bearing paleosol samples were obtained from drill cores and outcrops that contain referenced PT sections, to generate new siderite $\delta^{18}\text{O}$ data, and to combine with previously published data (Table 1, Fig. 2). Sample localities include eastern Australia (G. Mitchell and T. White, The Pennsylvania State University; G. Retallack, University of Oregon), Alaska (T. White, The Pennsylvania State University), Siberia (L. Elkins-Tanton, Arizona State University), and Antarctica (G. Retallack, University of Oregon). Samples from the North Slope of Alaska were collected from the East Simpson Test Well No. 1 (depths of 2278.1–2314.3 m) and Drew Point Test Well No. 1 National Petroleum Reserve drill cores (depths of 2380.6–2382.0 m) as referenced in Haywood (1983) and Brockway (1983), respectively. Samples from each of the other locations were collected from outcrops. All samples were cut into slabs roughly perpendicular to bedding and thin-sectioned to confirm the presence of siderite and detail the mineral assemblages within the paleosol matrix.

Two methods were employed for removing siderite from the paleosol. If the spherules had a diameter ≥ 1 mm, siderite was extracted from the paleosol using a microscope-mounted 0.5 mm drill bit. If the siderite was microcrystalline or too small for the drill bit to acquire a mostly pure sample, a magnetic separation method was used. In this method, the sample was ground with a mortar and pestle to 125–250 μm (120–60 mesh) and then separated with an ERIEZ HI-VI Model F magnetic cross-belt separator. Siderite is paramagnetic, meaning that it will form an internal induced magnetic field in the

direction of an externally applied magnetic field (Thompson and Oldfield, 1986). Ferrimagnetic mineral grains (magnetite) were subsequently removed from the extracted siderite with a magnet.

Approximately 0.2–0.6 mg of ground/drilled siderite was transferred into vials and loaded onto a GC PAL[®]. All of the samples were then reacted with phosphoric acid at 80 $^\circ\text{C}$ for as much as 24 h to liberate CO_2 . The CO_2 gas was pumped to and analyzed in a Thermo Scientific[™] Delta V[™] Plus isotope ratio mass spectrometer (IRMS), providing measurements for both $\delta^{18}\text{O}$ and $\delta^{13}\text{C}$ relative to VPDB. CaCO_3 standards used in the analyses include the certified working standards NBS 18 (−23.2‰) and NBS 19 (−2.20‰), as well as the Biogeochem house standard (−1.47‰), specifically utilized as an internal system check. All IRMS work was done at the Light Isotope Lab at the Light Isotopes in Metals and the Environment lab cluster (LIL-LIME) at The Pennsylvania State University.

All of the data were corrected for drift and instrument errors as well as fractionations that occurred during the analytical process, i.e., $\text{FeCO}_3\text{--CO}_2$ fractionation caused by the liberation of CO_2 from phosphoric acid, which is outlined by Carothers et al. (1988). At 80 $^\circ\text{C}$ the fractionation factor for $\text{FeCO}_3\text{--CO}_2$ is ~ 1.0099882 . This fractionation factor was folded into a two-point correction that was applied to all of the data in each set of samples run on the IRMS. NBS 18 and NBS 19 standards were analyzed by the IRMS twice before analyzing any samples. The standards were analyzed again halfway through the sample set, and once more at the end. All of the standard values measured for $\delta^{18}\text{O}$ and $\delta^{13}\text{C}$ throughout the run were averaged and compared to the true standard value relative to VPDB to formulate an equation that was used to correct all of the data in the run.

2.2. General circulation model

Paleosol siderite $\delta^{18}\text{O}$ data was compared to a modern GENESIS version 3.0 GCM (Alder et al., 2011) simulation and best fit line from filtered data of the IAEA/WMO network (Rozanski et al., 1993). The filtered gradients (shown in Fig. 5) represent low elevation sites < 300 m above sea level (masl), which host the settings where wetlands containing siderite are most likely to occur (Ludvigson et al., 1998; White et al., 2000). In addition to the modern simulation, five PT GENESIS simulations with different parameters (Table 2) were used to simulate surface temperature and $\delta^{18}\text{O}$ of precipitation. Siderite $\delta^{18}\text{O}$ was then derived from the model using the temperature-dependent siderite-water fractionation equation of Zhang et al. (2001) (Eq. (1)) in order to compare to the paleosol siderite $\delta^{18}\text{O}$ values.

Table 2
Parameters utilized in GENESIS simulations.

| Experiment/ simulation | pCO ₂ (ppm) | pCH ₄ (ppb) | pN ₂ O (ppb) | pCFC-11 (CCl ₃ F) (ppt) | pCFC-12 (CCl ₂ F ₂) (ppt) | Geography/ topography | Solar constant (W/ m ²) | Background aerosol optical depth | Maximum cloud droplet radius (μm) | Precipitation efficiency factor |
|-------------------------------|---------------------------|---------------------------|----------------------------|--|--|--------------------------|---|--|---|------------------------------------|
| (1) Modern | 355 | 1714 | 311 | 280 | 503 | Modern | 1367.0 | 0.14 | 10 | 1.0 |
| (2) 1 × PAL | 280 | 650 | 285 | n/a | n/a | Latest Permian | 1337.9 | n/a | 10 | 1.0 |
| (3) 4 × PAL | 1120 | 650 | 285 | n/a | n/a | Latest Permian | 1337.9 | n/a | 10 | 1.0 |
| (4) 4 × PAL reduced CCN | 1120 | 650 | 285 | n/a | n/a | Latest Permian | 1337.9 | n/a | 13 | 2.2 |
| (5) 12.7 × PAL | 3550 | 650 | 285 | n/a | n/a | Latest Permian | 1337.9 | n/a | 10 | 1.0 |
| (6) 12.7 × PAL reduced CCN | 3550 | 650 | 285 | n/a | n/a | Latest Permian | 1337.9 | n/a | 13 | 2.2 |

GENESIS consists of a coupled 18 layer, 3-D atmospheric GCM (AGCM) and land-surface model with a 50 m-thick slab ocean. Resolution for the AGCM is $3.75^\circ \times 3.75^\circ$ (T31) and $2^\circ \times 2^\circ$ for the surface model. Atmospheric gas concentrations for the modern simulation (1) are based on IPCC standards from 1991 to 1995 (IPCC, 1995), whereas gases other than CO₂ are prescribed as pre-industrial for PT simulations. Version 3.0 uses solar and thermal radiation code from the National Center for Atmospheric Research (NCAR) Community Climate Model 3 (CCM3) (Kiehl et al., 1998). PT simulations have a uniform diffusive ocean heat flux coefficient and no prescribed ocean currents. Earth orbital parameters are constant for all simulations with zero eccentricity and 23.5° obliquity. The land surface was specified as a uniform savannah-type biome. Late Permian geography and topography utilized in the model was developed by Ziegler et al. (1997) and was modified minimally to reflect updated paleogeographic reconstructions of Domeier and Torsvik (2014) (Fig. 2). Each simulation was run for 30 years, and results are monthly or annual averages over the last 10 years, to allow for spin-up of the mixed-layer ocean and to reduce interannual variability. An averaging period of 10 years has been used in many paleoclimatic studies with GENESIS (as cited above) and other GCMs, and is considered to accurately represent long-term model means after spin-up of slab-ocean temperatures.

The water isotopic components of the GENESIS GCM are described thoroughly in Mathieu et al. (2002). Although GENESIS v2.0 (Thompson and Pollard, 1997) was used in that study, the isotopic components are unchanged in version 3.0 used here. As in most isotope-enabled atmospheric GCMs, $^{18}\text{O}/^{16}\text{O}$ and D/H ratios are tracked explicitly in water vapor, cloud, precipitation, and surface-water reservoirs, with isotopic fractionation accounted for in transfers between these reservoirs. The proceeding section evaluates the veracity of GENESIS v3.0, particularly with regards to its effectiveness when modeling water isotopes.

3. Model evaluation

Modern climate results of the GENESIS v3.0 GCM (simulation 1) have been compared to observations in Thompson and Pollard (1997) for version 2.0 with a slab ocean. Although there have been no published validations for version 3.0 with a slab ocean, the quality of the modern simulation is similar to version 2.0. Alder et al. (2011) performed a detailed validation study for the modern climate with GENMOM, i.e., GENESIS v3.0 coupled with the Modular Ocean Model version 2 (MOM2). They were able to match surface temperature with observations at $\pm 5^\circ\text{C}$, with the largest positive anomalies in the Southern Ocean and largest negative anomalies in the Norwegian Sea. These temperature anomalies have been attributed to suppressed cold water upwelling and excessive sea ice, respectively. Annual precipitation amounts are most anomalous at low latitudes along the

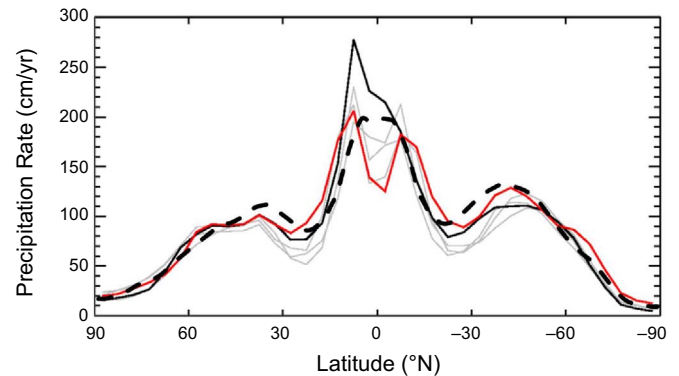


Fig. 3. Zonally averaged modern annual precipitation rates for models including GENMOM (red), IPCC AR4 (gray), and GENESIS v3.0 (black dashed line). Modern observations (black solid line) suggest higher precipitation rates at low latitudes than models. Figure modified from Alder et al. (2011). (For interpretation of the references to color in this figure legend, the reader is referred to the web version of this article.)

intertropical convergence zone (ITCZ), where underestimates of at least 150 cm occur in the Indian, western Pacific, and western Atlantic oceans. Overestimates of up to 150 cm occur in the eastern Pacific at 15°S . The precipitation anomalies in GENMOM coincide with similar regions in the three IPCC AR4 assessment models (Randall et al., 2007), the result of the development of a double-ITCZ, which is not observed in the modern. GENESIS v3.0 appears to remedy this issue, although still underestimates equatorial precipitation by at least 50 cm/yr (Fig. 3). Precipitation overestimates occur at mid latitudes, though they are minor, at ~ 10 – 20 cm/yr. Although this study does not couple GENESIS with an ocean model, we do not expect there to be drastic changes in model weaknesses. The lack of a dynamic ocean in GENESIS v3.0 may be a source of error, such as through overestimation of high-latitude temperatures (Zhou et al., 2008), though errors in model surface temperatures, if they are sensitive to ocean currents, would be more prevalent in cooler or modern simulations than in warm simulations because of the reduced thermal gradient and likely weakened or absent thermohaline circulation. The mostly anoxic and perhaps stratified ocean during the late Permian (Kajiura et al., 1994) probably had little effect on the distribution of surface temperatures, at least in the warmest simulations (4–6).

The previous version of GENESIS, version 2.0, did not include the atmospheric radiation code of NCAR CCM3, which is utilized in version 3.0. GENESIS v2.0 replicates modern observed precipitation $\delta^{18}\text{O}$ at low to mid latitudes with high accuracy, and does so reasonably well at high latitudes (Mathieu et al., 2002). Most discrepancies arise in Antarctica and Greenland and in elevated regions such as the Himalaya, Sierra Nevada, and south-central Africa (see Fig. 4 in Mathieu et al., 2002). GENESIS v2.0 underestimates depletions by 4–14‰ in

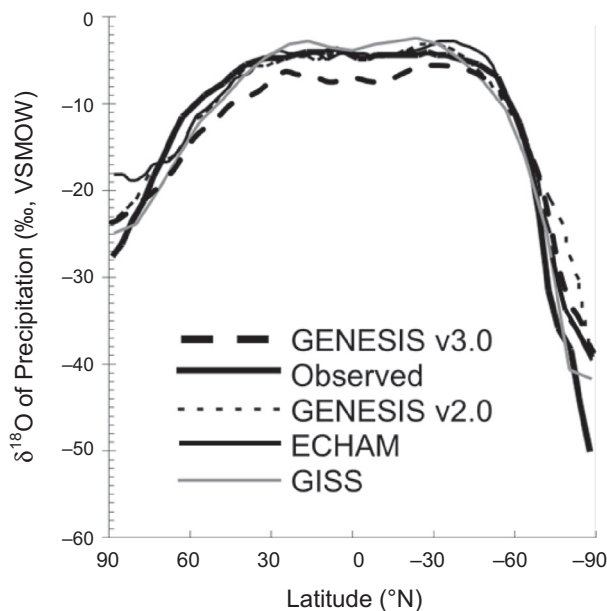


Fig. 4. Zonally averaged modern annual $\delta^{18}\text{O}$ of precipitation for various models and modern observations. GENESIS v3.0 (model used in this study) has significantly lower values at low latitudes, possibly the result of overestimating the spatial amount effect. Figure modified from Mathieu et al. (2002).

Greenland and Antarctica, respectively, and overestimates depletions by 2–14‰ at high elevations, most notably in the Himalaya and Tibetan Plateau. Mathieu et al. (2002) suggest that temperature anomalies, snow formation effects, or inadequate capture of dynamical effects (limited by the model's horizontal resolution) at steep high-latitude regions explain the precipitation $\delta^{18}\text{O}$ depletion underestimates. Excessive depletions at high elevations are explained by Mathieu et al. (2002) to be the result of altitude and temperature effects causing rainout – a common error in GCM's with relatively coarse horizontal resolutions. Model errors must be considered when interpreting the proxy data, although the topography that tends to produce errors in the modern simulation (steep elevation changes; e.g., Antarctica and the Himalaya) is not as prevalent in the PT because of the orogenic gap that began in the early Permian (Erwin, 1993; Windley, 1995).

GENESIS v3.0 simulates modern precipitation $\delta^{18}\text{O}$ reasonably well at high latitudes, and is comparable with other models (Fig. 4). At low latitudes, however, v3.0 is less accurate than v2.0 at simulating precipitation $\delta^{18}\text{O}$, with a depletion of $\sim 4\text{‰}$ relative to observations at the equator. This error occurred to a lesser extent in v2.0, possibly due to overestimation of the spatial amount effect, the spatial relationship between $\delta^{18}\text{O}$ of precipitation and rainfall amount, over low latitude oceans (Mathieu et al., 2002). Presumably its exacerbation in v3.0 is due to slight changes (probably in vertical profiles and mixing) stemming from the use of the NCAR CCM3 atmospheric radiation code, the only major physical change in v3.0 from v2.0. Although this error is significant with relation to the other models and modern observations reported in Mathieu et al. (2002), GENESIS v3.0, when filtered to report siderite $\delta^{18}\text{O}$ at low elevation (< 300 masl) to eliminate effects related to continentality, generally agrees well with modern filtered station data from Rozanski et al. (1993) converted to siderite values at latitudes $> 50^\circ$ (Fig. 5). Additionally, the model veracity is supported by the slope of the modern relationship between temperature and $\delta^{18}\text{O}$ of precipitation, where GENESIS v3.0 varies by only $\sim 6\%$ compared to modern observations reported in Rozanski et al. (1993) (Fig. 6C).

4. Results

4.1. Siderite

In Fig. 5, previously published PT siderite $\delta^{18}\text{O}$ at paleolatitudes greater than $\sim 55^\circ$ is depleted up to 10‰ below the filtered and non-filtered modern gradients extracted from the modern GENESIS simulation (1) and expected modern gradient derived from the IAEA/WMO network (Rozanski et al., 1993). The new data (see Fig. 5 and Table 3) is generally in agreement with the previously published data at comparable latitudes. Exceptions include North Slope, Alaska siderites, which plot at or above the modern siderite $\delta^{18}\text{O}$ gradient, and a subset of samples from the Sydney and southern Gunnedah Basins, which plot at the modern gradient. The variability of siderite $\delta^{18}\text{O}$ at $\sim 70^\circ$ paleolatitude is of bimodal character, with clustered data at -10‰ and ~ -18 to -20‰ . The slope of a linear regression (dashed, double-dotted line in Fig. 5) through the PT siderite $\delta^{18}\text{O}$ is about twice as steep (up to $\sim 0.5\text{‰}$ per degree latitude) compared to the meridional gradient of siderites from the PETM and Mid-Cretaceous (Fig. 1).

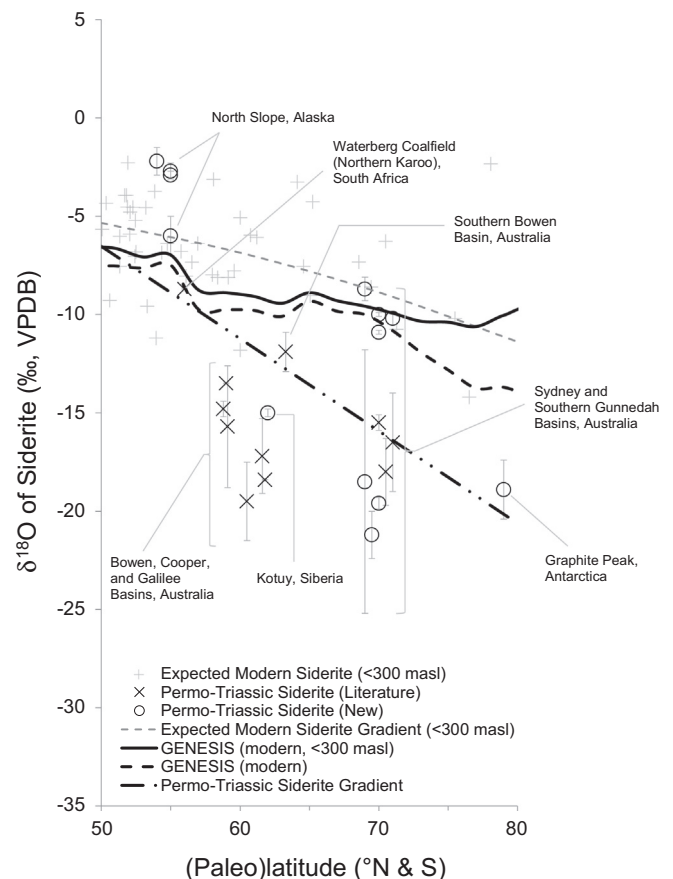


Fig. 5. Permo-Triassic siderite $\delta^{18}\text{O}$ data compared to the expected modern siderite gradient from Fig. 1 (gray dashed line), in addition to the modern GENESIS simulation (1), shown as a land only zonal mean (black dashed line) and a filtered land only zonal mean using data from < 300 masl (black solid line). The best fit line through the siderite data (black dash double dotted line) is significantly steeper over latitude than the modern estimates.

Table 3

Siderite from this study.

| Sample ^a | Location | n ^b | Paleolatitude (°N) ^c | Formation | Age | D/M ^d | Current (A) | $\delta^{18}\text{O}_{\text{VPDB}}/\text{‰}$ | $\delta^{13}\text{C}_{\text{VPDB}}/\text{‰}$ |
|---------------------|-------------------------------|----------------|---------------------------------|---------------------|-----------------|------------------|-------------|--|--|
| K08-13.7 | Kotuy, Siberia | 3 | 62 | Tungussskaya Series | Latest Permian | M | 1.1 | -15.0 ± 0.2 | $+1.6 \pm 0.2$ |
| ES7475 | North Slope, Alaska | 3 | 55 | Ivishak Fm. | Late P-Early Tr | D | – | -2.9 ± 0.2 | $+6.7 \pm 0.8$ |
| ES7476 | North Slope, Alaska | 4 | 55 | Ivishak Fm. | Late P-Early Tr | D | – | -2.7 ± 0.4 | $+5.1 \pm 0.2$ |
| ES7591 | North Slope, Alaska | 5 | 55 | Ivishak Fm. | Late Permian | D | – | -6.0 ± 1.0 | -10.1 ± 1.9 |
| DP7812.5 | North Slope, Alaska | 4 | 54 | Ivishak Fm. | Late P-Early Tr | D | – | -2.2 ± 0.7 | $+5.1 \pm 0.5$ |
| R1621 | Kerrabee, NSW, Australia | 3 | –69 | Digby Fm. | Griesbachian | M | 1.1 | -8.7 ± 0.6 | -1.8 ± 0.3 |
| R1625 | Kerrabee, NSW, Australia | 2 | –69 | Digby Fm. | Griesbachian | D | – | -18.5 ± 6.7 | -11.5 ± 4.8 |
| Aussiecoal | NSW, Australia | 6 | –69.5 | – | Late Permian | D/M | 1.3 | -21.2 ± 1.2 | -7.9 ± 2.4 |
| R395 | North Avalon, NSW, Australia | 2 | –70 | Newport Fm. | Spathian | D | – | -10.9 ± 0.1 | -6.1 ± 0.2 |
| R411 | Bilgola Beach, NSW, Australia | 2 | –70 | Garie Fm. | Smithian | D | – | -10.0 ± 0.1 | -15.5 ± 0.9 |
| P/T Aust | Bilgola Beach, NSW, Australia | 5 | –70 | Garie Fm. | Smithian | D | – | -19.6 ± 0.3 | -5.4 ± 0.5 |
| R1685 | Clifton, NSW, Australia | 6 | –71 | Coal Cliff SS | Changhsingian | D | – | -10.2 ± 0.3 | -7.0 ± 1.2 |
| R2008 | Graphite Peak, Antarctica | 3 | –79 | Buckley Fm. | Late Permian | M | 4.0 | -18.9 ± 1.5 | -6.4 ± 1.6 |

^a Sample names – K() from L. Elkins-Tanton; ES(), DP(), P/T Aust from T. White; R() from G. Retallack; Aussiecoal from G. Mitchell.^b Number of samples run in IRMS.^c Approximate PT paleolatitude (confidence $\pm 5^\circ$).^d D-drilled, M-magnetically separated, D/M-both methods.

4.2. Model

All six GENESIS simulations were parameterized according to Table 2. The name and/or number of each experiment/simulation referred to throughout the text correspond to those listed in Table 2. The following paragraphs discuss the major trends that exist among surface temperature, $\delta^{18}\text{O}$ of precipitation, precipitation rate, and model-derived siderite $\delta^{18}\text{O}$ for each of the simulations, shown in Figs. 6 and 7, with annual land-only and globally averaged values summarized in Table 4. Mean annual maps of surface temperature, $\delta^{18}\text{O}$ of precipitation, and precipitation rate for each simulation are presented in the Appendices (see supplementary information). Note that the sharp positive jumps that occur in PT land-only meridional profiles in Fig. 6A, B, and D between 80 and 90° latitude are the result of limited land coverage at high latitude, and not model artifacts or errors.

Fig. 6A shows the land-only zonal mean annual surface temperature gradient for each simulation. The most obvious difference is the reduction in PT thermal gradients relative to the modern. PT thermal gradients systematically increase across latitude with increasing $p\text{CO}_2$ or the reduction of CCN. Each PT thermal gradient differs by $\sim 25\text{--}30^\circ\text{C}$ between equator and pole. This is in contrast to the $45\text{--}70^\circ\text{C}$ modern thermal gradient. Mean annual temperatures for $4 \times \text{PAL}$ reduced CCN (4) are slightly warmer than the $12.7 \times \text{PAL}$ (5) simulation, which has normal cloud properties. Average land surface temperatures warm significantly more relative to globally averaged surface temperatures with increased $p\text{CO}_2$ or reduced CCN (Table 4).

PT land-only zonal mean annual $\delta^{18}\text{O}$ of precipitation gradients (Fig. 6B), like surface temperature, are significantly reduced relative to the modern. Unlike surface temperature, however, $\delta^{18}\text{O}$ gradients of precipitation shallow significantly with warmer mean annual global temperatures. For example, in the $1 \times \text{PAL}$ (2) simulation, the greatest difference in zonal mean annual $\delta^{18}\text{O}$ of precipitation between the equator and high latitudes is $\sim 8\text{--}13\text{‰}$, compared to just $\sim 4\text{--}6\text{‰}$ in the $12.7 \times \text{PAL}$ reduced CCN (6) simulation. The zonal mean annual $\delta^{18}\text{O}$ of precipitation at the equator also rises from $\sim -8\text{‰}$ to $\sim -4\text{‰}$ between the coolest (2) and warmest (6) PT simulation. Global mean annual values of precipitation $\delta^{18}\text{O}$ (Table 4) increase from -11.20‰

(2) to -6.74‰ (6) with proportionately more enrichment occurring over the ocean than on land.

An approximately linear relationship exists between precipitation $\delta^{18}\text{O}$ and temperature at mid- to high latitudes (Fig. 6C). The positive slopes of the PT gradients, taken from 40° to 90° latitude, are similar, varying at most between 0.351 for the $12.7 \times \text{PAL}$ reduced CCN (6) simulation and 0.597 for the $4 \times \text{PAL}$ (3) simulation. The modern relationship derived from Rozanski et al. (1993) and reported in White et al. (2001) has a slope of 0.416, compared to the GENESIS modern (1) simulation of 0.393, calculated from the linear portion between 40° and 70° latitude.

Mean annual land-only precipitation rates (Fig. 6D) for PT model experiments are $> 50\text{ cm/yr}$ lower at the equator than the modern. Warmer PT mean annual global temperatures lower mean annual precipitation rates at the equator by as much as 50 cm/yr between simulation 2 and 6. Unlike the modern, rates of PT precipitation are significantly higher at high latitudes, and the rates increase with increasing global mean annual temperature. For $12.7 \times \text{PAL}$ (5), $4 \times \text{PAL}$ reduced CCN (4), and $12.7 \times \text{PAL}$ reduced CCN (6) simulations, the land-only zonal mean annual precipitation rates at high latitudes are greater than at low latitude land sites. Like $\delta^{18}\text{O}$ of precipitation, precipitation rates over the ocean increase proportionately more than precipitation rates over land with increasing global mean annual warmth (Table 4).

The expected $\delta^{18}\text{O}$ content of siderite for each simulation is shown in Fig. 7. The maps in Fig. 7 include a precipitation-weighted annual zonal mean profile of siderite $\delta^{18}\text{O}$ (black profile line), and colored profiles that correspond to the siderite $\delta^{18}\text{O}$ had the siderite formed during a particular month. These monthly predictions are derived from the modeled zonal mean annual monthly surface temperature and $\delta^{18}\text{O}$ of precipitation using Eq. (1). PT siderites from most localities are $5\text{--}10\text{‰}$ more depleted than model predictions. Annual zonal mean profiles between each simulation do not differ tremendously, however the monthly siderite $\delta^{18}\text{O}$ profiles are less variable in warmer simulations.

At high latitudes, a region of south-central Gondwana is more depleted in simulation 3 ($4 \times \text{PAL}$), reaching siderite $\delta^{18}\text{O}$ values of at

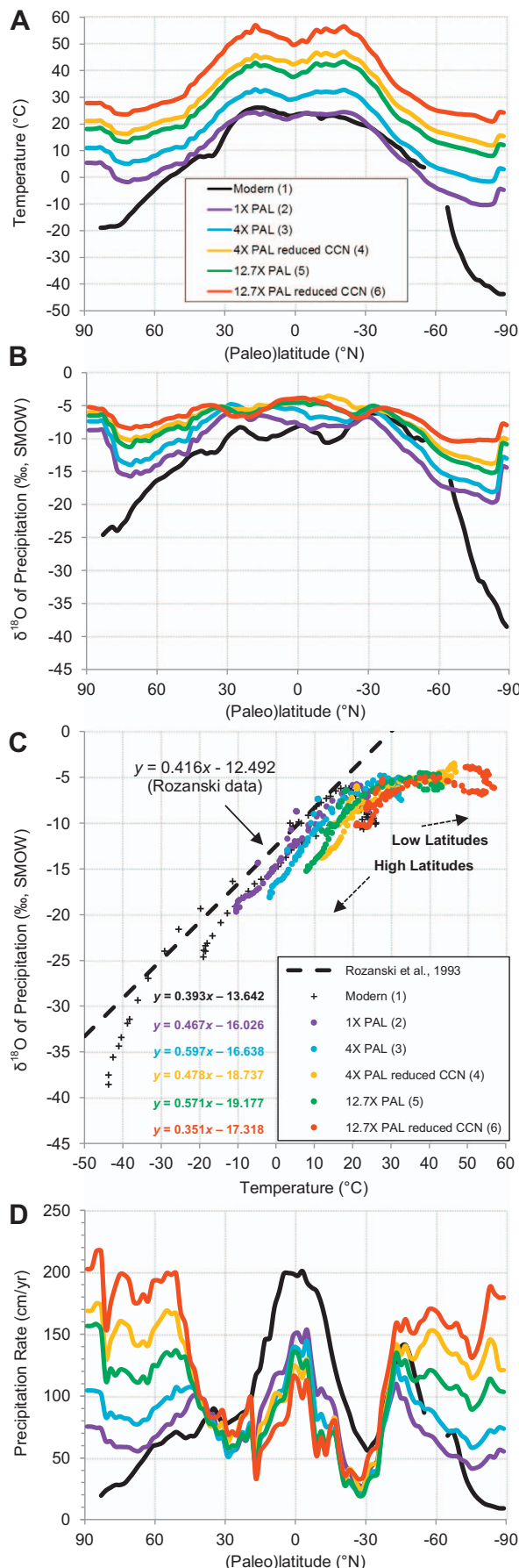


Fig. 6. (A) Land-only zonal mean annual plot of surface temperature for each model simulation. The legend in (A) is also applicable to (B) and (D). (B) Land-only zonal mean annual plot of $\delta^{18}\text{O}$ of precipitation for each model simulation. (C) Plot of $\delta^{18}\text{O}$ of precipitation (B) vs. temperature (A). The behavior of both of these variables determines siderite $\delta^{18}\text{O}$. The equations listed to the left of the plot legend are best fit lines of the positively sloping regions at high latitude. The modern relationship of Rozanski et al. (1993) (black dashed line) matches well with the GENESIS-derived modern relationship. (D) Land-only zonal mean annual plot of precipitation rate for each model simulation. Low latitudes become drier and high latitudes wetter under warmer PT climate simulations.

least -13‰ , compared to -11 to -12‰ in simulation 2 ($1 \times \text{PAL}$) (Fig. 7). This feature is also present in simulation 5 ($12.7 \times \text{PAL}$). With the exception of this local feature, which is further discussed in Section 5.2 below, siderite $\delta^{18}\text{O}$ values at high-latitude continental sites generally become further enriched with increasing global mean annual temperature, whereas more depleted values occur between 15 and 40° paleolatitude. This is amplified in reduced CCN simulations. Warmer mean annual global temperatures lower siderite $\delta^{18}\text{O}$ values at coastal sites, with the lowest values in eastern Gondwana occurring in simulation 5 ($12.7 \times \text{PAL}$). This is curtailed in the reduced CCN simulations. In contrast to $\delta^{18}\text{O}$ of precipitation, globally averaged annual siderite $\delta^{18}\text{O}$ is generally depleted with higher global mean annual temperatures, falling from -7.75 to -8.84‰ between (2) and (6) (Table 4), with most of the depletion occurring at low- to mid-latitudes in simulations 4, 5, and 6.

5. Discussion and interpretations

5.1. Preferred model simulation

The reason that precipitation-weighted annual zonal mean siderite $\delta^{18}\text{O}$ profiles are markedly similar among all five PT simulations (Fig. 7), particularly from mid- to high latitude, is due to two inter-related mechanisms; one, the similar linear relationships between surface temperature and $\delta^{18}\text{O}$ of precipitation (Fig. 6C), and two, the subsequent scaling that occurs between the increase in water vapor $\delta^{18}\text{O}$ and decrease in siderite-water fractionation when global mean annual temperature increases. This scaling can be influenced by isotope effects on the local scale. Thus, in order to properly select a preferred PT model simulation, variations in model-derived siderite $\delta^{18}\text{O}$ must be inspected on a site-specific basis, that is, extracting the siderite $\delta^{18}\text{O}$ value at a site's particular model grid cell (Fig. 8).

In Fig. 8, the $12.7 \times \text{PAL}$ (5) simulation best represents the $\sim -10\text{‰}$ siderites in the Sydney and Gunnedah Basins (within 1‰), whereas simulations 4, 5, and 6 ($4 \times \text{PAL}$ reduced CCN, $12.7 \times \text{PAL}$, and $12.7 \times \text{PAL}$ reduced CCN) best represent Waterberg Coalfield, Karoo Basin ($< 1\text{‰}$). The relatively more depleted North Slope sample (ES7591) agrees best with simulation 6 ($12.7 \times \text{PAL}$ reduced CCN), though it is also acceptable within error for simulations 4 ($4 \times \text{PAL}$ reduced CCN) and 5 ($12.7 \times \text{PAL}$). Relatively more enriched North Slope samples plot $> 1\text{‰}$ above simulation 2 ($1 \times \text{PAL}$), perhaps due to seawater mixing during their formation. Although the majority of paleosol siderite samples (75%) fall well below model siderite $\delta^{18}\text{O}$ values, of the five PT model simulations, only $12.7 \times \text{PAL}$ (5) best agrees with paleosol siderite $\delta^{18}\text{O}$ in both coastal and continental settings (Fig. 8B).

In addition to its agreement with the siderite data, $12.7 \times \text{PAL}$ (5) also produces surface temperatures that are comparable to those suggested in the literature for the PT boundary. Kiehl and Shields (2005) argue that relatively low $p\text{CO}_2$, such as in the $1 \times \text{PAL}$ (2) and $4 \times \text{PAL}$ (3) simulations, was too cold at high latitude to support the flora preserved from these regions. Kidder and Worsley (2004) suggest that temperatures around the PT boundary were 35°C at the equator and 15°C at the poles, with a global annual average value of 25°C . Only the $12.7 \times \text{PAL}$ (5) simulation is consistent with the arguments presented in

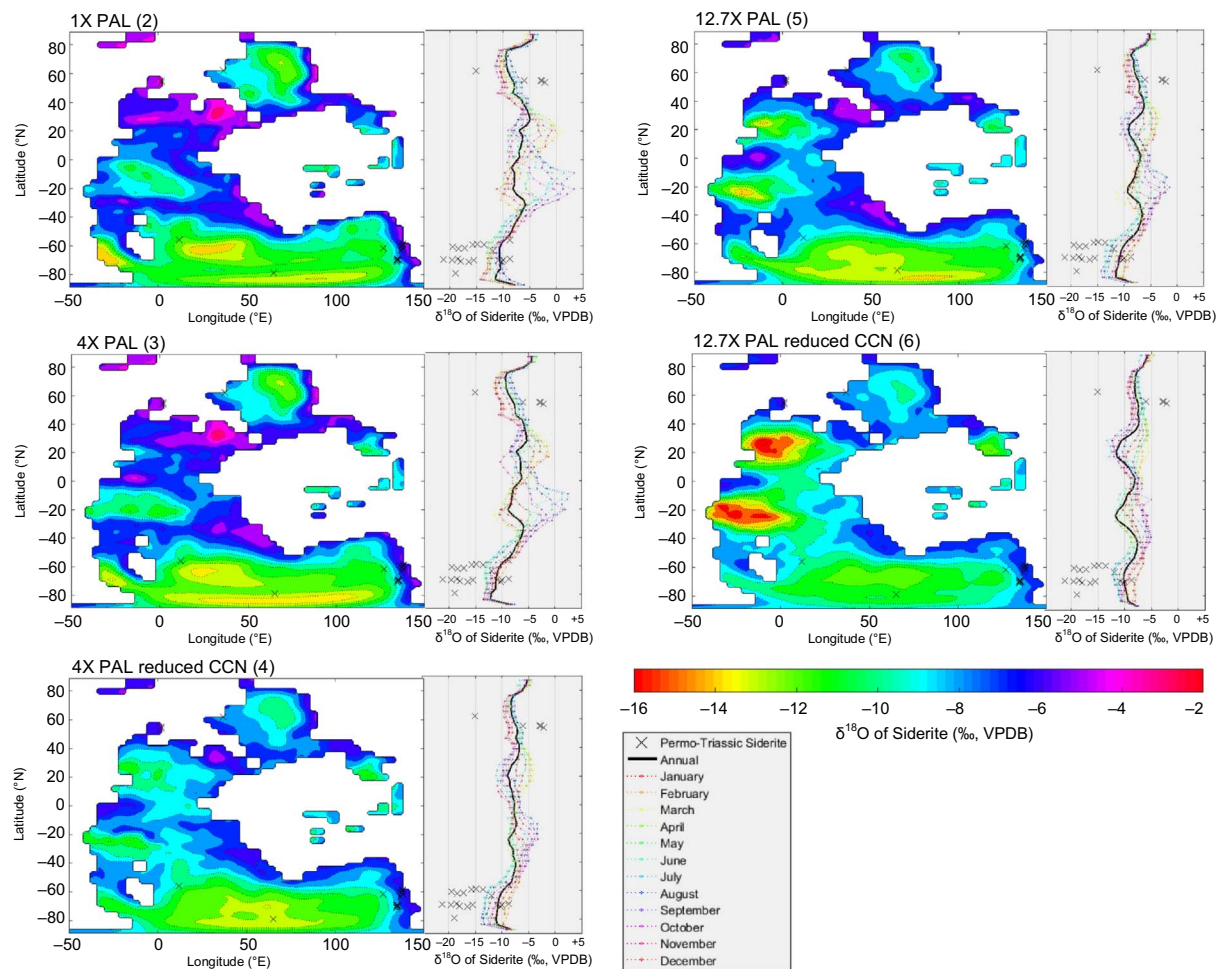


Fig. 7. Mean annual $\delta^{18}\text{O}$ of siderite maps for each Permo-Triassic model simulation with zonal mean annual precipitation-weighted meridional siderite $\delta^{18}\text{O}$ gradients (black line) and mean monthly siderite $\delta^{18}\text{O}$ (colored lines) compared to PT siderite $\delta^{18}\text{O}$ data (x's). Map contours are spaced every 1‰.

Table 4

Average annual values calculated globally, as land only, and as differences between each, where applicable.

| | | 1 × PAL (2) | 4 × PAL (3) | 4 × PAL reduced CCN (4) | 12.7 × PAL (5) | 12.7 × PAL reduced CCN (6) |
|---|--------------------|-------------|-------------|-------------------------|----------------|----------------------------|
| Surface temperature (°C) | Land only | 9.37 | 16.70 | 29.47 | 25.84 | 37.70 |
| | Global | 14.79 | 20.10 | 29.62 | 26.96 | 35.87 |
| | Global – Land only | 5.42 | 3.40 | 0.15 | 1.12 | –1.83 |
| $\delta^{18}\text{O}$ of Precipitation (‰, VSMOW) | Land only | –11.20 | –9.60 | –7.46 | –8.05 | –6.74 |
| | Global | –8.30 | –7.34 | –6.10 | –6.32 | –5.50 |
| | Global – Land only | +2.90 | +2.26 | +1.36 | +1.73 | +1.24 |
| Precipitation Rate (cm/yr) | Land only | 75.04 | 81.62 | 112.09 | 96.78 | 126.45 |
| | Global | 108.97 | 120.99 | 158.35 | 138.82 | 175.01 |
| | Global – Land only | 33.93 | 39.37 | 46.26 | 42.04 | 48.56 |
| $\delta^{18}\text{O}$ of Siderite (‰, VPDB) | Land only | –7.75 | –7.74 | –8.12 | –8.02 | –8.84 |

both Kiehl and Shields (2005) and Kidder and Worsley (2004), with an average global annual temperature of $\sim 27^\circ\text{C}$ (Table 4). Reduced CCN simulations are $\sim 5^\circ\text{C}$ (simulation 4) to $\sim 10^\circ\text{C}$ (simulation 6) too warm on average in comparison to PT temperature estimates.

On the basis of its agreement with siderite $\delta^{18}\text{O}$ and temperature estimates for the PT boundary, simulation 5 (12.7 × PAL) is the preferred model run. A calculation for precipitation $\delta^{18}\text{O}$ using the model surface temperatures of simulation 5 (Fig. 8C), shows that the mean annual $\delta^{18}\text{O}$ of precipitation would have to be 8–13‰ lower than what was simulated in the model to match the most depleted siderite values. Instead, if calculating for surface temperature using the modeled $\delta^{18}\text{O}$ of precipitation values, the paleosol siderite $\delta^{18}\text{O}$ could be obtained if

mean annual temperatures were as much as 80°C warmer than model predictions, arguably unrealistic levels (Fig. 8D). The following sections explore the reasons why the models were unable to generate low siderite $\delta^{18}\text{O}$, and present the possible mechanisms that can explain high-latitude siderite depletions during hothouse intervals.

5.2. Weather patterns in southern Gondwana

A narrow region of depleted siderite $\delta^{18}\text{O}$ along the Gondwanides range in south-central Gondwana, especially prominent in the 4 × PAL (3) simulation and 12.7 × PAL (5) simulation (Fig. 7), is likely related to the development of a wedge of dry air in winter through spring (Jun-

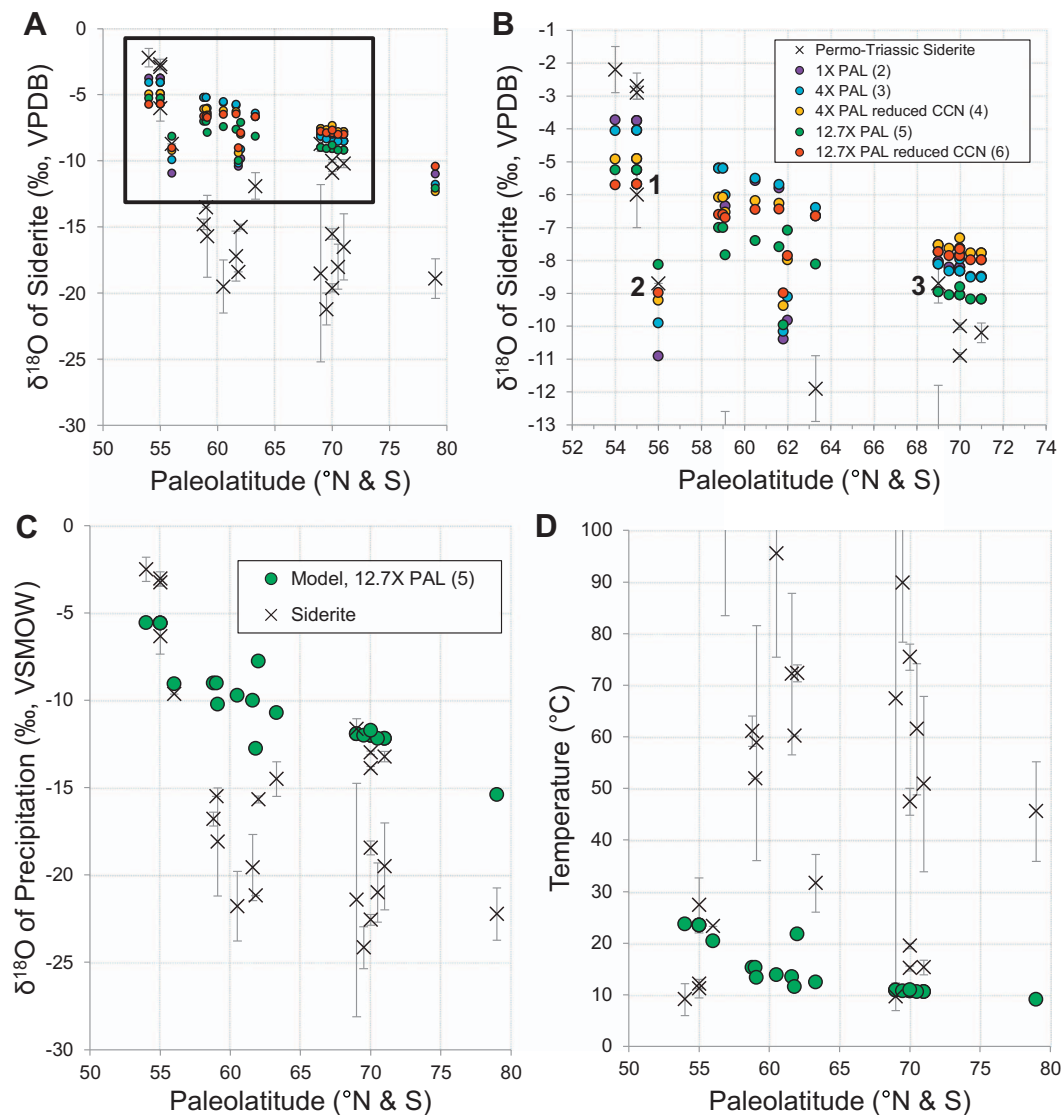


Fig. 8. (A) Site-specific comparison of siderite data and model simulations. (B) is inset of (A), with legend applying to (A) and (B). Simulation 5 matches high latitude samples the best, although the majority of samples are too depleted to be explained by the mean annual model siderite $\delta^{18}\text{O}$ values. Three samples overlap with model simulation results: (1) ES7591, North Slope, Alaska; (2) Waterberg Coalfield, South Africa from Faure et al. (1995); (3) R1621, Kerrabee, southern Gunnedah Basin, New South Wales, Australia. (C) Siderite samples calculated for $\delta^{18}\text{O}$ of precipitation using preferred model temperatures. Legend in (C) also applies to (D). (D) Siderite-derived surface temperatures using preferred model $\delta^{18}\text{O}$ of precipitation.

Oct) with the onset of a weak southerly to westerly flow (Fig. 9A). This 1 to 2‰ lowering of siderite $\delta^{18}\text{O}$ relative to the 1 × PAL (2) simulation, particularly for the Graphite Peak, Antarctica location (black circle in Fig. 9), is considered to be mostly the result of continentality effects. Graphite Peak is located ~1200 km from its closest PT paleoshoreline directly to the south; however, airmasses corresponding with the lowering of siderite $\delta^{18}\text{O}$ had traveled over land from ~1600 km (Sep-Oct) to > 3200 km (Jun–Aug).

Continentality also results in the 12.7 × PAL (5) simulation producing the lowest model derived siderite $\delta^{18}\text{O}$ in eastern Australia of −11.5‰ in July. An offshore wind throughout the austral autumn and winter brought moisture from the tropics across northeastern Gondwana towards the eastern Australian basins.

Relative enrichments in eastern Australia siderite $\delta^{18}\text{O}$ occurred during the rainy season, when a monsoonal circulation developed (Fig. 9). Beginning in late spring (Nov), a northwest wind brought tropical moisture from the southern Neotethys across eastern Gondwana, which was forced to rainout along the foreland basins due to the topographic barrier to the south and east. The monsoon peaked in the summer (Dec–Jan) when there was a direct onshore flow from the east-

northeast. This resulted in total rainfall amounts of over 30 cm in the Sydney Basin (black star in Fig. 9) and over 50 cm in the Bowen Basin (due north of the Sydney Basin at ~55–60°S) from Nov–Jan. These rates of precipitation are expected to significantly lower siderite $\delta^{18}\text{O}$, but instead, the rains originated close to the coast due to high rates of evaporation, and thus had a high initial $\delta^{18}\text{O}$ of ~−4‰. The oxygen isotopic content of the parent vapor is much too high for the amount effect to have significant bearing on the siderite $\delta^{18}\text{O}$. Model derived siderite $\delta^{18}\text{O}$ in the Sydney Basin is −10.8‰ at the start of the monsoon, and rises to −8.5‰ at its conclusion in February (Fig. 9B). The moisture associated with the monsoon is comparable to the strongest region of the modern North American monsoon, where up to 40 cm of rainfall occurs in northwestern Mexico over a three month period (Adams and Comrie, 1997).

PT models using similar boundary conditions also produce high rates of precipitation in eastern Gondwana during the austral summer (Winguth and Winguth, 2013). Geological evidence from latest Permian and earliest Triassic paleosols indicate mean annual precipitation rates between 700 and 1400 mm/yr in the Sydney Basin (Retallack, 1997, 1999) and 400 to 1100 mm/yr for late Permian Antarctic paleosols

(Retallack and Krull, 1999). GENESIS simulation 5 ($12.7 \times \text{PAL}$) agrees with these rainfall estimates, and thus may support the modeled strength of the monsoon, with $\sim 1160 \text{ mm/yr}$ over the Sydney Basin and $\sim 700 \text{ mm/yr}$ at Graphite Peak, Antarctica.

Seasonal weather patterns across southern Gondwana do not produce low enough precipitation $\delta^{18}\text{O}$ to form the lowest siderite $\delta^{18}\text{O}$ values. Additionally, the precipitation source from the monsoon is mostly local, relatively enriched in $\delta^{18}\text{O}$, and does not produce a noticeable amount effect in the model simulations. Therefore, we cannot suggest amount effects related to seasonal rainfall in eastern Australia, or continentality effects in Antarctica, to explain the majority of the sample siderite $\delta^{18}\text{O}$.

5.3. Biological cloud feedback

It was hypothesized that reducing the number of CCN in the atmosphere would allow for an extreme amount effect, capable of producing low $\delta^{18}\text{O}$ of precipitation and subsequently, low siderite $\delta^{18}\text{O}$ during the summer. In the GENESIS simulations, globally averaged overland precipitation rates increase 26% between $12.7 \times \text{PAL}$ (5) and $12.7 \times \text{PAL}$ reduced CCN (6) and 31 % between $4 \times \text{PAL}$ (3) and $4 \times \text{PAL}$ reduced CCN (4), while mean annual overland temperatures also increase 46 % between $12.7 \times \text{PAL}$ (5) and $12.7 \times \text{PAL}$ reduced CCN (6) and 76% between $4 \times \text{PAL}$ (3) and $4 \times \text{PAL}$ reduced CCN (4) (Table 4). The differences in precipitation rate with temperature are so

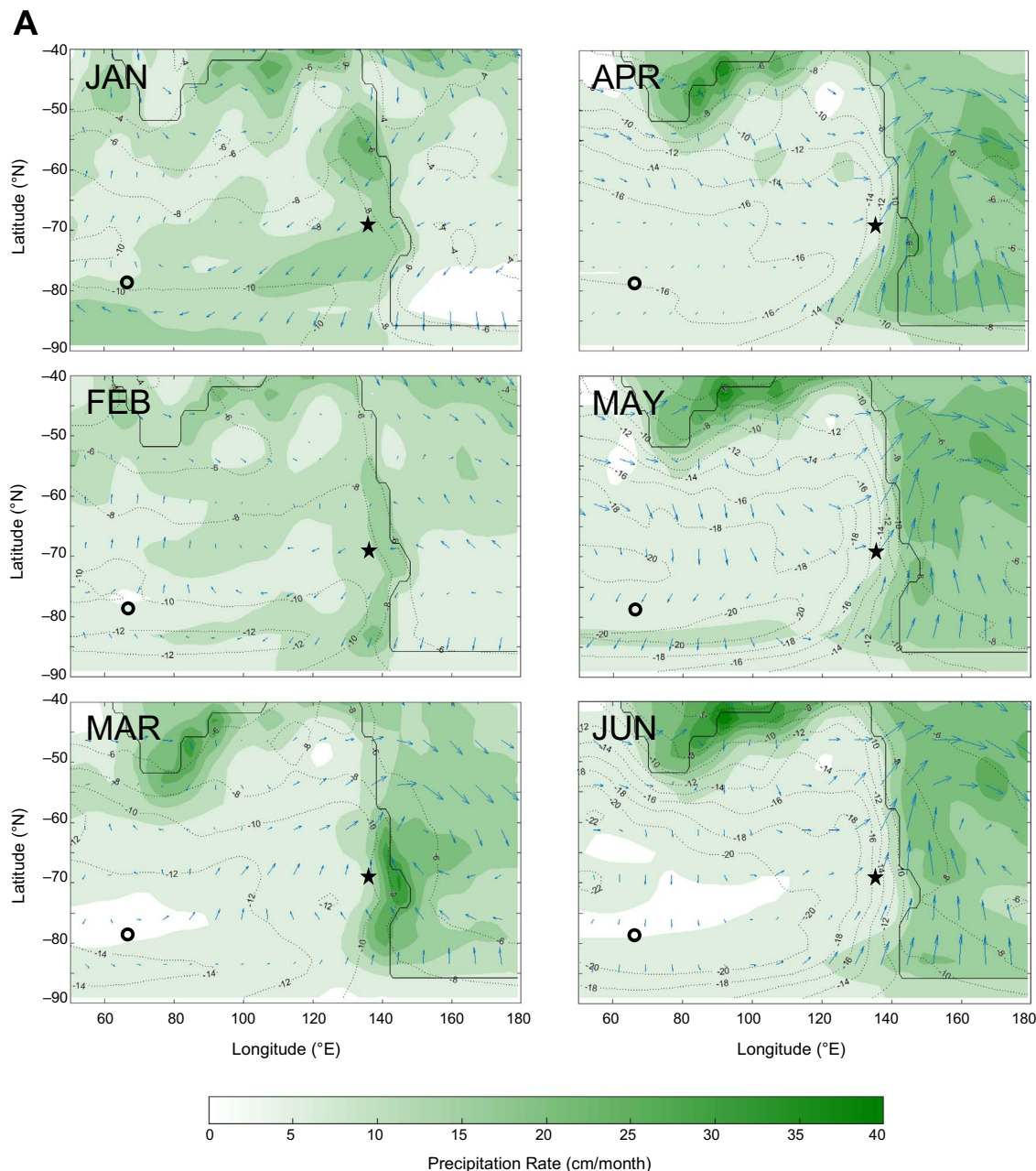


Fig. 9. (A) Mean monthly precipitation rate maps for southeastern Gondwana. Included on the maps are contours of mean monthly precipitation $\delta^{18}\text{O}$ (‰, VSMOW), and wind direction (blue arrows). The black circle and star indicate the Graphite Peak, Antarctica location and Sydney Basin, Australia region, respectively. Note the development of the monsoon in eastern Gondwana in early summer. There is little depletion in precipitation $\delta^{18}\text{O}$ related to the amount effect during the monsoon season. Most of the depleted precipitation $\delta^{18}\text{O}$ values occur in the winter when continentality effects and low temperatures are in control. (B) Plots of siderite $\delta^{18}\text{O}$ (‰, VPDB) derived monthly from the model (black line), compared to sample values (red dotted lines) for select locations. The months highlighted in purple indicate the presence of the monsoon. The lowest model derived siderite $\delta^{18}\text{O}$ values occur during the winter, whereas the highest occur during the monsoon. (For interpretation of the references to color in this figure legend, the reader is referred to the web version of this article.)

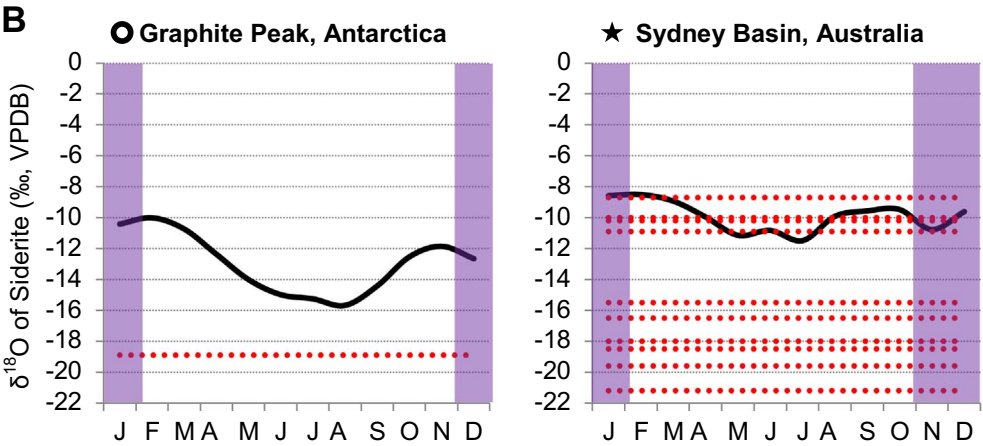
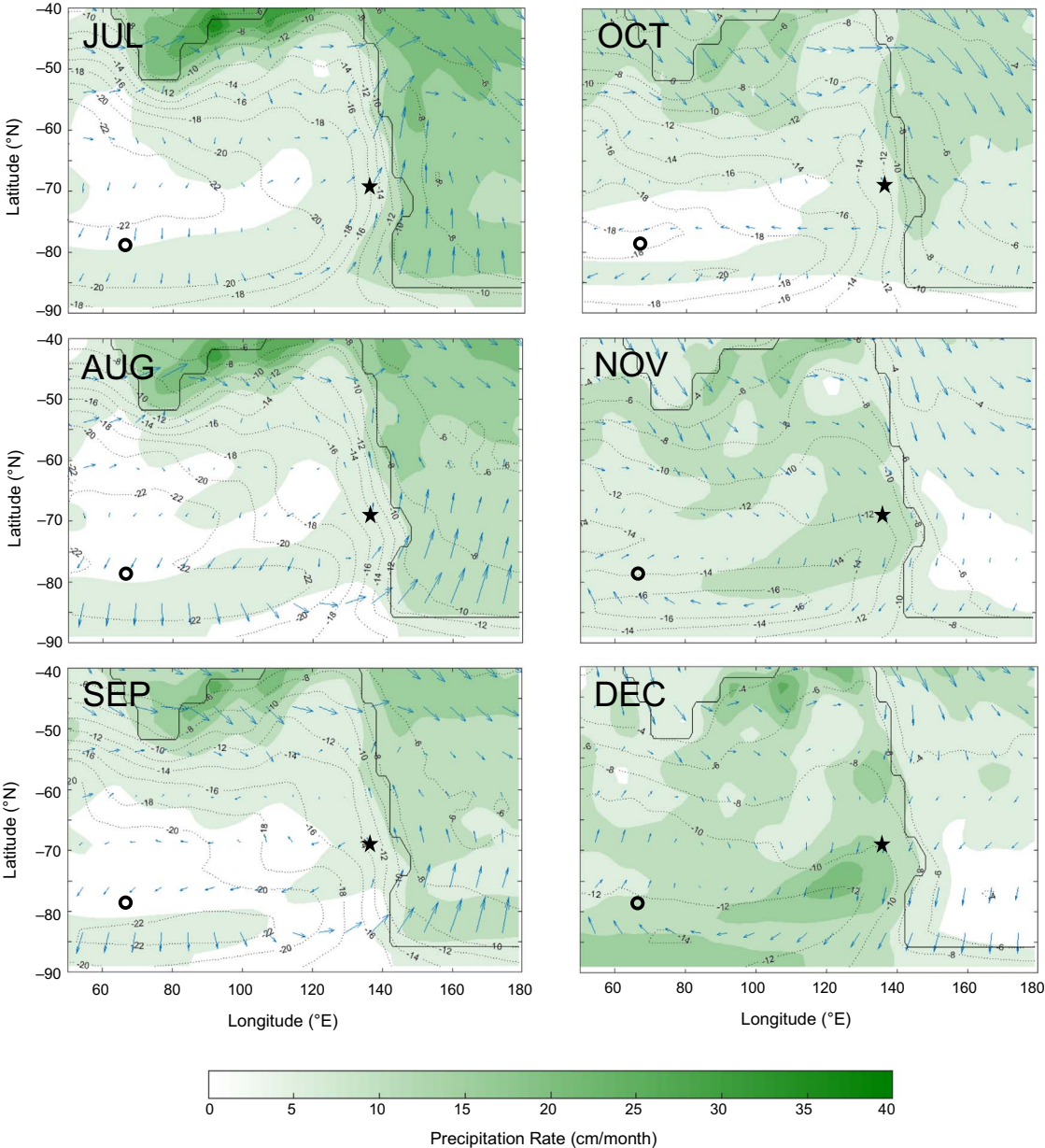


Fig. 9. (continued)

small because the ability to transport moisture over large distances is lessened. The highest rates of rainfall increase in reduced CCN simulations occur over the ocean and along the coast. This would seem to be ideal for our hypothesis, because it would suggest greater amount effects in the localities where siderite is likely to occur. However, coastal sites experience higher mean annual $\delta^{18}\text{O}$ of precipitation (see Appendix 2 in the supplementary information) because precipitation is sourced locally and evaporation rates are higher, thus the vapor is relatively enriched in $\delta^{18}\text{O}$.

Although Kump and Pollard (2008) argue that the CCN effect can match hothouse climate temperatures suggested by marine and terrestrial proxies, it is not viable to explain the low $\delta^{18}\text{O}$ of the siderite proxy. Warming associated with lowering Earth's albedo is too significant, thus creating a very high saturation vapor pressure and water vapor of much too high $\delta^{18}\text{O}$. Amount effects from enhanced coastal precipitation rates are not significant enough in the model to lower the $\delta^{18}\text{O}$ content of the parent vapor.

5.4. Local isotope effects and seasonal siderite formation

5.4.1. Seasonal variability

The occurrence of distinct, repetitive, siderite-rich laminae in ancient lacustrine sediments are suggested to have formed during seasonal changes in lake pore water chemistry (Bahrig, 1989), or during favorable conditions, such as “calm” depositional periods when sedimentation rates were low (Lojka et al., 2009, 2010). Lojka et al. (2010) found that siderites occurring in littoral sediments from a Late Pennsylvanian lake had a wide range in $\delta^{18}\text{O}$ content of $> 7\%$, compared to a range of $\sim 3.7\%$ for those forming in limnetic deposits. They suspect that marginal lake sediments are subjected to more isotopic variability because of differences in local hydrologic inputs. Lakes with variable authigenic carbonate $\delta^{18}\text{O}$ can also indicate seasonal differences in the precipitation/evaporation ratio (Leng and Marshall, 2004).

The effect of high evaporation rates and increased aridity between the latest Permian and earliest Triassic has been observed as a $\sim 5\%$ increase in soil carbonate $\delta^{18}\text{O}$ in the Karoo Basin of South Africa (MacLeod et al., 2017). If the wetlands the siderites had formed in experienced high rates of evaporation during their growth, heavier $\delta^{18}\text{O}$ values than what was modeled in GENESIS simulation 5 ($12.7 \times \text{PAL}$) are expected, but this is not the case. Additionally, the siderites are generally well-constrained and feature large ranges of $\delta^{18}\text{O}$ in sections of stratigraphy of similar ages (Bulli coal and overlying Coal Cliff sandstone, both latest Permian according to Metcalfe et al., 2015) and in the same formations (earliest Triassic Digby Formation and early Triassic Garie Formation). It is likely that the mechanisms producing the ranges in siderite $\delta^{18}\text{O}$ were present across the PT boundary. Because the majority of the siderites have low $\delta^{18}\text{O}$, this suggests that seasonal variation in the precipitation/evaporation ratio is not significant. High relative humidity year-round at high latitudes likely reduced seasonal evaporation variability. However, different precipitation sources and water inputs could be involved in lowering wetland pore water $\delta^{18}\text{O}$ from the local meteoric signal and may explain the spread of siderite $\delta^{18}\text{O}$ from eastern Australia. Siderite is known to occur in deposits that have been interpreted as seasonal wetlands (Wright et al., 2000), and so the temperature and water $\delta^{18}\text{O}$ during the season that siderite is forming can impart biases that we may suspect as a mean annual signal.

5.4.2. High altitude drainage

Low $\delta^{18}\text{O}$ siderites from the PT Rewan Group (southern Bowen Basin, Australia) were first speculated by Baker et al. (1996) to have formed in soil waters derived from high altitude precipitation from nearby mountain ranges. Fricke et al. (2010) illustrate a bimodal distribution of aragonite $\delta^{18}\text{O}$ from unionid bivalves in pond facies of the Sevier Mountains of North America during the Late Cretaceous. They suggest that their observed $\sim 8.5\%$ difference is a result of wetlands

recharged from high-elevation-derived trunk rivers and streams relative to wetlands recharged from local basin waters. They conclude that regions affected by seasonal highland precipitation do not reflect global trends in oxygen isotope ratios. The similar spread of Fricke et al. (2010) observed in the siderites from the Sydney Basin may be due to comparable processes, and would suggest that anomalously low $\delta^{18}\text{O}$ siderites may have formed in waters not derived solely from local precipitation. If this is the case, the subset of samples that are relatively less depleted may reflect the local meteoric signal. This would suggest that PT wetlands which preserved a mean annual precipitation $\delta^{18}\text{O}$ signal are either uncommon, or that siderite growth is more likely to have occurred during a particular season.

5.4.3. Snowmelt-recharge mechanism

High-latitude samples, including those from eastern Australia, Antarctica, and Siberia are all located near PT mountain ranges and could have acquired precipitation either locally, via drainage from the mountains, or via drainage from the continental interior. It is possible to reconstruct the highly depleted $\delta^{18}\text{O}$ values of these high-latitude siderites by invoking seasonal wetland recharge, where summertime temperatures and winter-derived precipitation are responsible for wetland conditions during siderite growth (Fig. 10). This requires high-latitude settings with large-area continental interiors, in addition to either frozen ground during winter months or limited available precipitation during the summer. Under these conditions, winter snow and ice melt can provide the depleted $\delta^{18}\text{O}$ necessary to match observed high-latitude depleted siderite $\delta^{18}\text{O}$. Modeled winter snowpack (not shown) in continental Gondwana can exceed 40 cm, with potentially more at high elevations not resolved in the model. Despite eastern Australia and Antarctica receiving most of their modeled rainfall in the summer, melting winter precipitation from inland and upland sources can be a significant contributor to total net recharge. Inland recharge is likely a significant component of ground water, and is reflected in the $\delta^{18}\text{O}$ composition of pedogenic carbonates, such as meteoric calcite cements (Hays and Grossman, 1991). In Siberia, however, modeled snowfall is much less (~ 8 cm) and probably has little role in the isotopic composition of summer groundwater. Instead, high altitude precipitation and drainage from the Uralian Range immediately south and east of the Kotuy River site could explain the observed low $\delta^{18}\text{O}$ values.

The last glacial stage of the late Paleozoic, the P4 glacial interval (Fielding et al., 2008), may have persisted as late as ~ 254.5 Ma (Metcalfe et al., 2015). Ice during P4 was confined to the elevated Lachlan and Thomson orogens to the south and west of the Bowen and Sydney basins (Fielding et al., 2008). It is possible that after the termination of this last Permian glacial interval, vestiges of small alpine glaciers may have released waters that had recharged the wetlands in which siderite precipitated. Although we did not include glacial ice in GENESIS, we can track the simulated recharge of wetland soils month-to-month to see if there are any relationships between melting snow, high rates of rainfall, and runoff at particular grid cells in a region of interest, and consider that below.

Soil moisture recharge calculated by GENESIS, defined as an increase in the fractional liquid content of ice-free soil pores relative to saturation, suggests that the northern Karoo Basin; North Slope, Alaska; and Kotuy, Siberia received most of their soil water content from local precipitation, equable to mean annual precipitation $\delta^{18}\text{O}$, whereas the Sydney Basin and Graphite Peak, Antarctica soils received most of their recharge during periods that are not directly related to local rainfall, most likely from spring snowmelt (Fig. 10). Freezing conditions in the wintertime for the Sydney Basin and Graphite Peak coincide with the driest soil conditions on average, and most runoff, suggesting that there is snow cover over these regions in the model during those timespans. This supports a mechanism for spring soil moisture recharge preceding the summer monsoon. GENESIS does not include the transport or flow of water across grid cells and therefore does not capture the drainage from high elevations that would feed into basins. Better hydrological

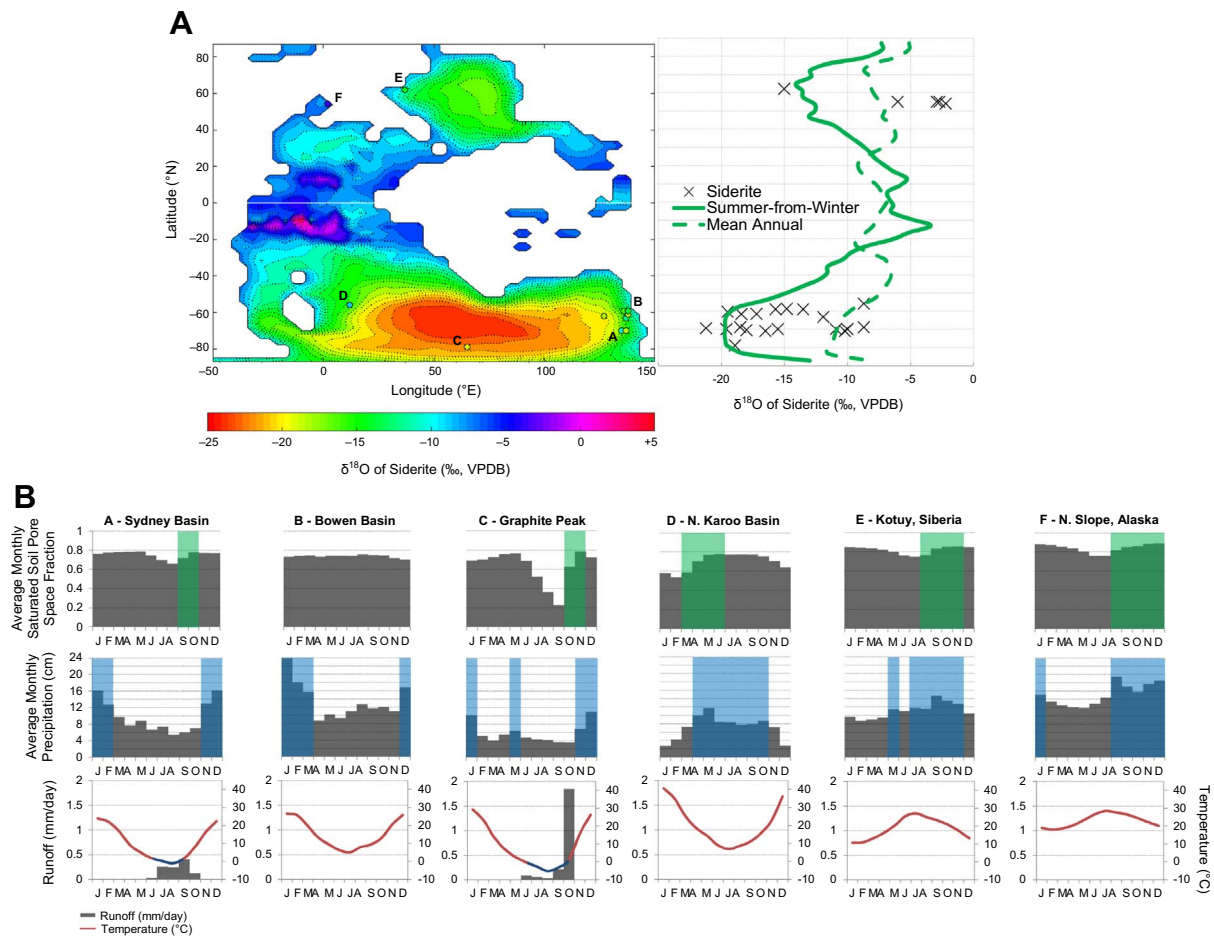


Fig. 10. (A) Summer-from-winter simulation utilizing January and July mean temperatures and $\delta^{18}\text{O}$ of precipitation from simulation 5 ($12.7 \times \text{PAL}$). Contours on map are spaced 1‰. Colored dots are siderite sample locales with siderite $\delta^{18}\text{O}$ averages color-coded to the scalebar. Letters coincide with regional monthly averages of saturated soil pore space fraction, precipitation, runoff, and temperature in (B). The zonal mean profile to the right of the map shows that a summer-from-winter formation mechanism can explain anomalously low siderite $\delta^{18}\text{O}$. (B) Green boxes in the saturated soil pore space fraction bar graphs demarcate months of significant soil moisture recharge. Blue boxes in the precipitation bar graphs are the months of $> 50\%$ the average monthly rainfall amount. When the green and blue boxes overlap on the same month(s), this suggests recharge associated with direct precipitation. When the boxes are offset, as they are in A and C, this suggests a different source, in this case snowmelt. Snowmelt is the likely source because runoff in these regions is highest when the average monthly temperature rises from below freezing (blue) to above (red). The release of snowmelt into these regions precedes the beginning of the rainy season/monsoon. (For interpretation of the references to color in this figure legend, the reader is referred to the web version of this article.)

models and advanced soil models could remedy this issue, but would likely further reinforce this argument.

We favor this process for explaining high-latitude PT siderites because the model supports the mechanisms that could lead to a pulse of low $\delta^{18}\text{O}$ waters into wetlands during the spring or summer. Modern studies indicate that regions located near mountains receive a considerable amount ($> 80\%$) of their groundwater budget from high altitude river water (e.g., Yeh et al., 2014) and that this water is depleted with respect to local precipitation $\delta^{18}\text{O}$ (e.g., Seeyan and Merkel, 2014). Therefore, we would expect that groundwater-fed or mountain river-fed wetlands contain a significant amount of water with low $\delta^{18}\text{O}$, depleted because of the altitude effect. Siderite growth is expected to occur during warmer months when CO_2 production from microbial processes and plant root respiration is highest, which is also the time when siderite-water fractionation is small. Higher microbial activity can help catalyze the reduction of ferric iron (e.g. Peretyazhko and Sposito, 2005) providing a source of ferrous iron to form siderite. In warmer global climates the seasonality at high latitudes is reduced, so annual productivity probably lasted longer than during the modern.

6. Conclusions

Paleosol siderite $\delta^{18}\text{O}$ from samples collected around the PT

boundary show anomalously low values at high latitudes and agree with those reported previously from the literature. The meridional siderite $\delta^{18}\text{O}$ gradient is just as or steeper than other hothouse intervals. The geographic pattern of a subset of samples that are relatively less depleted in $\delta^{18}\text{O}$ tend to agree with GENESIS model simulations. The $12.7 \times \text{PAL}$ (5) simulation achieves the temperatures required to support Gondwanan fossil evidence and produces the most depleted mean annual values for near coastal sites at high latitude, caused by a sufficient lowering of precipitation $\delta^{18}\text{O}$.

Reducing cloud albedo and enhancing rainout efficiency by reducing CCN number density and increasing droplet size do not produce sufficiently depleted siderite $\delta^{18}\text{O}$ because the associated temperature increase is too great, and precipitation $\delta^{18}\text{O}$ too high. Although the temperatures produced by the biological cloud feedback mechanism agree with proxy data from select hothouse periods, depleted siderite $\delta^{18}\text{O}$ from these intervals cannot be justified.

A monsoonal circulation that developed in the austral summer in eastern Gondwana did not produce a significant amount effect. The most significant lowering of siderite $\delta^{18}\text{O}$ occurred during the winter, where the combination of low temperatures and a southeast flow from the tropics brought moisture across eastern Gondwana to the Australian and Antarctic foreland basins, resulting in a lowering of precipitation $\delta^{18}\text{O}$ because of the continentality effect.

It is most probable that local effects, such as drainage into paleowetlands from mountains or seasonal siderite formation, where low $\delta^{18}\text{O}$ snow or ice melt contributed to spring/summer recharge, are responsible for low siderite $\delta^{18}\text{O}$ of at least -20‰ at high latitudes. Warm summer temperatures and low winter precipitation $\delta^{18}\text{O}$ provided the ingredients necessary to produce a majority of the depleted siderite $\delta^{18}\text{O}$ values. It is thus a requirement that there either be nearby high topography that allows for the drainage of melting frozen precipitation, or cold enough temperatures during the winter to deposit snow over siderite-producing wetlands. Our study shows that a PT model simulation with $12.7 \times \text{PAL CO}_2$ meets these criteria, and suggests that wetlands received a burst of recharge preceding the monsoon season.

Some important questions remain – to what extent did winter precipitation control the oxygen isotopic ratios of PT wetlands, and do the isotopically distinct siderites of the Sydney Basin represent different wetland types controlled by different hydrologic inputs/outputs, or separate time intervals when snow was more or less common? Additional sampling of well-constrained PT boundary paleosol siderites will help to further explain the hydrologic cycle and paleowetland hydrology during Earth's most severe episode of global climate change.

Supplementary data to this article can be found online at <https://doi.org/10.1016/j.palaeo.2017.11.062>.

Acknowledgements

We thank L. Elkins-Tanton, G. Retallack, and G. Mitchell for providing some of the samples for this research. We would also like to thank the two anonymous reviewers who offered feedback that greatly enhanced the quality of this paper. Financial support provided by the National Science Foundation EAR-0807744, 424-07 67G4 and by a Grant-In-Aid of Research from Sigma Xi, The Scientific Research Society.

References

- Adams, D.K., Comrie, A.C., 1997. The North American monsoon. *Bull. Am. Meteorol. Soc.* 78, 2197–2213.
- Alder, J.R., Hostetler, S.W., Pollard, D., Schmittner, A., 2011. Evaluation of a present-day climate simulation with a new coupled atmosphere-ocean model GENMOM. *Geosci. Model Dev. Discuss.* 4, 69–83. <http://dx.doi.org/10.5194/gmdd-3-1697-2010>.
- Andreae, M.O., 2007. Aerosols before pollution. *Science* 315, 50–51. <http://dx.doi.org/10.1126/science.1136529>.
- Bahrig, B., 1989. Stable isotope composition of siderite as an indicator of the paleoenvironmental history of oil shale lakes. *Palaeogeogr. Palaeoclimatol. Palaeoecol.* 70, 139–151.
- Baker, J.C., Kassan, J., Hamilton, P.J., 1996. Early diagenetic siderite as an indicator of depositional environment in the Triassic Rewan Group, southern Bowen Basin, eastern Australia. *Sedimentology* 43, 77–88.
- Bohren, C.F., 1985. Comment on “Cloud optical thickness feedbacks in the CO_2 climate problem” by Richard Somerville and L.A. Remer. *J. Geophys. Res.* 90, 5867.
- Botz, R.W., Hunt, J.W., Smith, J.W., 1986. Isotope geochemistry of minerals in Australian bituminous coal. *J. Sediment. Res.* 56, 99–111. <http://dx.doi.org/10.1306/212F8896-2B24-11D7-8648000102C1865D>.
- Brockway, R.G., 1983. Geological Report: Drew Point Test Well No. 1.
- Carothers, W.W., Adami, L.H., Rosenbauer, R.J., 1988. Experimental oxygen isotope fractionation between siderite-water and phosphoric acid liberated CO_2 -siderite. *Geochim. Cosmochim. Acta* 52, 2445–2450.
- Charlson, R.J., Lovelock, J.E., Andreae, M.O., Warren, S.G., 1987. Oceanic phytoplankton, atmospheric sulphur, cloud albedo and climate. *Nature* 326, 655–661. <http://dx.doi.org/10.1038/326655a0>.
- Domeier, M., Torsvik, T.H., 2014. Plate tectonics in the late Paleozoic. *Geosci. Front.* 5, 303–350. <http://dx.doi.org/10.1016/j.gsf.2014.01.002>.
- Erwin, D.H., 1993. *The Great Paleozoic Crisis: Life and Death in the Permian*. Columbia University Press, New York, NY, United States.
- Faure, K., Harris, C., Willis, J.P., 1995. A profound meteoric water influence on genesis in the permian waterberg coalfield, South Africa: evidence from stable isotopes. *J. Sediment. Res.* A65, 605–613. <http://dx.doi.org/10.1017/CBO9781107415324.004>.
- Faure, K., Dreyer, J.C., Willis, J.P., 1996. The Grootegeluk Formation in the Waterberg Coalfield, South Africa; facies, palaeoenvironment and thermal history; evidence from organic and clastic matter. *Int. J. Coal Geol.* 29, 147–186.
- Fielding, C.R., Frank, T.D., Birgenheier, L.P., Rygel, M.C., Jones, A.T., Roberts, J., 2008. Stratigraphic imprint of the Late Palaeozoic Ice Age in eastern Australia: a record of alternating glacial and nonglacial climate regime. *J. Geol. Soc. Lond.* 165, 129–140.
- Fricke, H.C., Foreman, B.Z., Sewall, J.O., 2010. Integrated climate model-oxygen isotope evidence for a North American monsoon during the Late Cretaceous. *Earth Planet. Sci. Lett.* 289, 11–21. <http://dx.doi.org/10.1016/j.epsl.2009.10.018>.
- Gabitov, R.I., Watson, E.B., Sadekov, A., 2012. Oxygen isotope fractionation between calcite and fluid as a function of growth rate and temperature: an in situ study. *Chem. Geol.* 306–307, 92–102. <http://dx.doi.org/10.1016/j.chemgeo.2012.02.021>.
- Gould, K.W., Smith, J.W., 1979. The genesis and isotopic composition of carbonates associated with some permian australian coals. *Chem. Geol.* 24, 137–150.
- Hays, P.D., Grossman, E.L., 1991. Oxygen isotopes in meteoric calcite cements as indicators of continental paleoclimate. *Geology* 19, 441–444.
- Haywood, H., 1983. Geological Report: East Simpson Test Well No. 1.
- IPCC, 1995. *Climate Change 1995: A Report of the Intergovernmental Panel on Climate Change*. IPCC Second Assess. 63.
- Kajiwar, Y., Yamakita, S., Ishida, K., Ishiga, H., Imai, A., 1994. Development of a largely anoxic stratified ocean and its temporary massive mixing at the Permian/Triassic boundary supported by the sulfur isotopic record. *Palaeogeogr. Palaeoclimatol. Palaeoecol.* 111, 367–379. [http://dx.doi.org/10.1016/0031-0182\(94\)90072-8](http://dx.doi.org/10.1016/0031-0182(94)90072-8).
- Kele, S., Özkul, M., Fórizs, I., Gökgöz, A., Baykara, M.O., Alçiçek, M.C., Németh, T., 2011. Stable isotope geochemical study of Pamukkale travertines: new evidences of low-temperature non-equilibrium calcite-water fractionation. *Sediment. Geol.* 238, 191–212. <http://dx.doi.org/10.1016/j.sedgeo.2011.04.015>.
- Kerminen, V.M., Paramonov, M., Anttila, T., Riipinen, I., Fountoukis, C., Korhonen, H., Asmi, E., Laakso, L., Lihavainen, H., Swietlicki, E., Svenningsson, B., Asmi, A., Pandis, S.N., Kulmala, M., Petäjä, T., 2012. Cloud condensation nuclei production associated with atmospheric nucleation: a synthesis based on existing literature and new results. *Atmos. Chem. Phys.* 12, 12037–12059. <http://dx.doi.org/10.5194/acp-12-12037-2012>.
- Kidder, D.L., Worsley, T.R., 2004. Causes and consequences of extreme Permo-Triassic warming to globally equable climate and relation to the Permo-Triassic extinction and recovery. *Palaeogeogr. Palaeoclimatol. Palaeoecol.* 203, 207–237. [http://dx.doi.org/10.1016/S0031-0182\(03\)00667-9](http://dx.doi.org/10.1016/S0031-0182(03)00667-9).
- Kiehl, J.T., Shields, C.A., 2005. Climate simulation of the latest Permian: implications for mass extinction. *Geology* 33, 757–760. <http://dx.doi.org/10.1130/G21654.1>.
- Kiehl, J.T., Hack, J.J., Hurrell, J.W., 1998. The energy budget of the NCAR Community climate model: CCM3. *J. Clim.* 11, 1151–1178. [http://dx.doi.org/10.1175/1520-0442\(1998\)011<1151:TEBOTN>2.0.CO;2](http://dx.doi.org/10.1175/1520-0442(1998)011<1151:TEBOTN>2.0.CO;2).
- Krishnan, S., Pagani, M., Huber, M., Sluijs, A., 2014. High latitude hydrological changes during the Eocene Thermal Maximum 2. *Earth Planet. Sci. Lett.* 404, 167–177. <http://dx.doi.org/10.1016/j.epsl.2014.07.029>.
- Kump, L.R., Pollard, D., 2008. Amplification of Cretaceous warmth by biological cloud feedbacks. *Science* 320, 195 (80–).
- Leng, M.J., Marshall, J.D., 2004. Palaeoclimate interpretation of stable isotope data from lake sediment archives. *Quat. Sci. Rev.* 23, 811–831. <http://dx.doi.org/10.1016/j.quascirev.2003.06.012>.
- Lojka, R., Drábková, J., Zajíč, J., Sýkorová, I., Francu, J., Bláhová, A., Grygar, T., 2009. Climate variability in the Stephanian B based on environmental record of the Mšec Lake deposits (Kladno-Rakovník Basin, Czech Republic). *Palaeogeogr. Palaeoclimatol. Palaeoecol.* 280, 78–93. <http://dx.doi.org/10.1016/j.palaeo.2009.06.001>.
- Lojka, R., Sykora, I., Laurin, J., Matysova, P., Grygar, T.M., 2010. Lacustrine couplet-lamination: evidence for Late Pennsylvanian seasonality in central equatorial Pangaea (Stephanian B, Mšec Member, Central and Western Bohemian basins). *Bull. Geosci.* 85, 709–733. <http://dx.doi.org/10.3140/bull.geosci.1210>.
- Ludvigson, G.A., González, L.A., Metzger, R.A., Witzke, B.J., Brenner, R.L., Murillo, A.P., White, T.S., 1998. Meteoric sphaerosiderite lines and their use for paleohydrology and paleoclimatology. *Geology* 26, 1039–1042. [http://dx.doi.org/10.1130/0091-7613\(1998\)026<1039:MSLATU>2.3.CO;2](http://dx.doi.org/10.1130/0091-7613(1998)026<1039:MSLATU>2.3.CO;2).
- MacLeod, K.G., Quinton, P.C., Bassett, D.J., 2017. Warming and increased aridity during the earliest Triassic in the Karoo Basin, South Africa. *Geology* 45, 483–486. <http://dx.doi.org/10.1130/G38957.1>.
- Mathieu, R., Pollard, D., Cole, J.E., White, J.W.C., Webb, R.S., Thompson, S.L., 2002. Simulation of stable water isotope variations by the GENESIS GCM for modern conditions. *J. Geophys. Res.* 107, 1–18. <http://dx.doi.org/10.1029/2001JD900255>.
- Metcalfe, I., Crowley, J.L., Nicoll, R.S., Schmitz, M., 2015. High-precision U-Pb CA-TIMS calibration of Middle Permian to Lower Triassic sequences, mass extinction and extreme climate-change in eastern Australian Gondwana. *Gondwana Res.* 28, 61–81. <http://dx.doi.org/10.1016/j.gr.2014.09.002>.
- Passy, S.R., 2014. The habit and origin of siderite spherules in the Eocene coal-bearing Prestfjall Formation, Faroe Islands. *Int. J. Coal Geol.* 122, 76–90. <http://dx.doi.org/10.1016/j.coal.2013.12.009>.
- Peretyazhko, T., Sposito, G., 2005. Iron(III) reduction and phosphorous solubilization in humid tropical forest soils. *Geochim. Cosmochim. Acta* 69, 3643–3652. <http://dx.doi.org/10.1016/j.gca.2005.03.045>.
- Poulsen, C.J., Pollard, D., White, T.S., 2007. General circulation model simulation of the $\delta^{18}\text{O}$ content of continental precipitation in the middle Cretaceous: a model-proxy comparison. *Geology* 35, 199–202. <http://dx.doi.org/10.1130/G23343A.1>.
- Randall, D.A., Wood, R.A., Bony, S., Colman, R., Fichefet, T., Fyfe, J., Kattsov, V., Pitman, A., Shukla, J., Srinivasan, J., Stouffer, R.J., Sumi, A., Taylor, K.E., 2007. Climate models and their evaluation. In: Solomon, S., Qin, D., Manning, M., Chen, Z., Marquis, M., Averyt, K.B., Tignor, M., Miller, H.L. (Eds.), *Climate Change 2007: The Physical Science Basis. Contribution of Working Group I to the Fourth Assessment Report of the Intergovernmental Panel on Climate Change*. Cambridge University Press, Cambridge, United Kingdom and New York, NY, USA.
- Retallack, G.J., 1997. Palaeosols in the upper Narrabeen Group of New South Wales as evidence of Early Triassic palaeoenvironments without exact modern analogues. *Aust. J. Earth Sci.* 44, 185–201.
- Retallack, G.J., 1999. Postapocalyptic greenhouse paleoclimate revealed by earliest

- Triassic paleosols in the Sydney Basin, Australia. *Bull. Geol. Soc. Am.* 111, 52–70. [http://dx.doi.org/10.1130/0016-7606\(1999\)111<0052:PGPRBE>2.3.CO;2](http://dx.doi.org/10.1130/0016-7606(1999)111<0052:PGPRBE>2.3.CO;2).
- Retallack, G.J., Krull, E.S., 1999. Landscape ecological shift at the Permian-Triassic boundary in Antarctica. *Aust. J. Earth Sci.* 46, 785–812. <http://dx.doi.org/10.1046/j.1440-0952.1999.00745.x>.
- Rozanski, K., Araguás-Araguás, L., Gonfiantini, R., 1993. Isotopic patterns in modern global precipitation. *Clim. Change Cont. Isot. Rec.* 78, 1–36. <http://dx.doi.org/10.1029/GM078p0001>.
- Seeyan, S., Merkel, B., 2014. Determination of recharge by means of isotopes and water chemistry in Shaqlawa-Harrir Basin, Kurdistan Region, Iraq. *Hydrol. Curr. Res.* 5, 179. <http://dx.doi.org/10.4172/2157-7587.1000179>.
- Speelman, E.N., Sewall, J.O., Noone, D., Huber, M., von der Heydt, A., Damsté, J.S., Reichert, G.J., 2010. Modeling the influence of a reduced equator-to-pole sea surface temperature gradient on the distribution of water isotopes in the Early/Middle Eocene. *Earth Planet. Sci. Lett.* 298, 57–65. <http://dx.doi.org/10.1016/j.epsl.2010.07.026>.
- Suarez, M.B., González, L.A., Ludvigson, G.A., 2011. Quantification of a greenhouse hydrologic cycle from equatorial to polar latitudes: the mid-Cretaceous water bearer revisited. *Palaeogeogr. Palaeoclimatol. Palaeoecol.* 307, 301–312.
- Thompson, R., Oldfield, F., 1986. *Environmental Magnetism*. Allen & Unwin, London.
- Thompson, S.L., Pollard, D., 1997. Greenland and Antarctic mass balances for present and doubled atmospheric CO₂ from the GENESIS version-2 global climate model. *J. Clim.* 10, 871–900. [http://dx.doi.org/10.1175/1520-0442\(1997\)010<0871:GAAMB>2.0.CO;2](http://dx.doi.org/10.1175/1520-0442(1997)010<0871:GAAMB>2.0.CO;2).
- Ufnar, D.F., González, L.A., Ludvigson, G.A., Brenner, R.L., Witzke, B.J., 2002. The mid-Cretaceous water bearer: isotope mass balance quantification of the Albian hydrologic cycle. *Palaeogeogr. Palaeoclimatol. Palaeoecol.* 188, 51–71. [http://dx.doi.org/10.1016/S0031-0182\(02\)00530-8](http://dx.doi.org/10.1016/S0031-0182(02)00530-8).
- Ufnar, D.F., Ludvigson, G.A., González, L.A., Brenner, R.L., Witzke, B.J., 2004a. High latitude meteoric $\delta^{18}\text{O}$ compositions: paleosol siderite in the Middle Cretaceous Nanushuk Formation, North Slope, Alaska. *Bull. Geol. Soc. Am.* 116, 463–473. <http://dx.doi.org/10.1130/B25289.1>.
- Ufnar, D.F., González, L.A., Ludvigson, G.A., Brenner, R.L., Witzke, B.J., 2004b. Evidence for increased latent heat transport during the Cretaceous (Albian) greenhouse warming. *Geology* 32, 1049–1052. <http://dx.doi.org/10.1130/G20828.1>.
- Uysal, I.T., Golding, S.D., Glickson, M., 2000. Petrographic and isotope constraints on the origin of authigenic carbonate minerals and the associated fluid evolution in late Permian coal measures, Bowen Basin, (Queensland), Australia. *Sediment. Geol.* 136, 189–206.
- White, T.S., Witzke, B.J., Ludvigson, G.A., 2000. Evidence for an Albian Hudson arm connection between the Cretaceous Western Interior Seaway of North America and the Labrador Sea. *Bull. Geol. Soc. Am.* 112, 1342–1355. [http://dx.doi.org/10.1130/0016-7606\(2000\)112<1342:EFAAHA>2.0.CO;2](http://dx.doi.org/10.1130/0016-7606(2000)112<1342:EFAAHA>2.0.CO;2).
- White, T.S., Gonzalez, L., Ludvigson, G.A., Poulsen, C.J., 2001. Middle Cretaceous greenhouse hydrologic cycle of North America. *Geology* 29, 363–366. [http://dx.doi.org/10.1130/0091-7613\(2001\)029<0363:Mcghco>2.0.CO;2](http://dx.doi.org/10.1130/0091-7613(2001)029<0363:Mcghco>2.0.CO;2).
- White, T., Bradley, D., Haeussler, P., Rowley, D.B., 2017. Late Paleocene-Early Eocene paleosols and a new measure of the transport distance of Alaska's Yakutat terrane. *J. Geol.* 125, 113–123.
- Windley, B.F., 1995. *The Evolving Continents*. John Wiley and Sons, New York.
- Winguth, A., Winguth, C., 2013. Precession-driven monsoon variability at the Permian-Triassic boundary - implications for anoxia and the mass extinction. *Glob. Planet. Chang.* 105, 160–170. <http://dx.doi.org/10.1016/j.gloplacha.2012.06.006>.
- Winguth, A.M.E., Shields, C.A., Winguth, C., 2015. Transition into a Hothouse World at the Permian-Triassic boundary-a model study. *Palaeogeogr. Palaeoclimatol. Palaeoecol.* 440, 316–327. <http://dx.doi.org/10.1016/j.palaeo.2015.09.008>.
- Winnick, M.J., Caves, J.K., Chamberlain, C.P., 2015. A mechanistic analysis of early Eocene latitudinal gradients of isotopes in precipitation. *Geophys. Res. Lett.* 42, 8216–8224. <http://dx.doi.org/10.1002/2015GL064829>. (Received).
- Wright, V.P., Taylor, K.G., Beck, V.H., 2000. The paleohydrology of Lower Cretaceous seasonal wetlands, Isle of Wight, southern England. *J. Sediment. Res.* 70, 619–632.
- Yeh, H., Lin, H., Lee, C., Hsu, K., Wu, C., 2014. Identifying seasonal groundwater recharge using environmental stable isotopes. *Water* 6, 2849–2861. <http://dx.doi.org/10.3390/w6102849>.
- Zhang, C.L., Horita, J., Cole, D.R., Zhou, J., Lovley, D.R., Phelps, T.J., 2001. Temperature-dependent oxygen and carbon isotope fractionations of biogenic siderite. *Geochim. Cosmochim. Acta* 65, 2257–2271. [http://dx.doi.org/10.1016/S0016-7037\(01\)00596-8](http://dx.doi.org/10.1016/S0016-7037(01)00596-8).
- Zhou, J., Poulsen, C.J., Pollard, D., White, T.S., 2008. Simulation of modern and middle Cretaceous marine $\delta^{18}\text{O}$ with an ocean-atmosphere general circulation model. *Paleoceanography* 23, 1–11. <http://dx.doi.org/10.1029/2008PA001596>.
- Ziegler, A.M., Hulver, M.L., Rowley, D.B., 1997. Permian world topography and climate. In: Martini, I.P. (Ed.), *Late Glacial and Postglacial Environmental Changes: Quaternary, Carboniferous-Permian and Proterozoic*. Oxford University Press, Oxford, pp. 111–146.